

Viscoelastic film flows over an inclined substrate with sinusoidal topography. II. Linear stability analysis

D. Pettas,¹ G. Karapetsas,² Y. Dimakopoulos,¹ and J. Tsamopoulos^{1,*}

¹*Laboratory of Fluid Mechanics and Rheology, Department of Chemical Engineering, University of Patras, Patras GR-26500, Greece*

²*Department of Chemical Engineering, Aristotle University of Thessaloniki, Thessaloniki GR-54124, Greece*



(Received 3 June 2019; published 8 August 2019)

The linear hydrodynamic stability of a film of viscoelastic fluid flowing down an inclined wavy surface is studied. We investigate the stability of the flow with respect to infinitesimal two- and three-dimensional (2D and 3D) disturbances and employ the Floquet-Bloch theory to examine the effect of periodic disturbances of any wavelength. The study is based on the numerical solution of the momentum equations along with the Phan-Thien–Tanner (PTT) model to account for material viscoelasticity. The generalized eigenvalue problem is solved using Arnoldi's algorithm, in a Newton-like implementation in order to calculate faster the critical conditions for the onset of the instability. Our results are in excellent agreement with the previous experimental and theoretical results in the case of Newtonian liquids flowing over flat and undulating substrates and viscoelastic liquids over flat substrates. We present detailed stability maps for finite amplitude of the wall corrugations and a wide range of material parameters. Our calculations indicate that fluid elasticity is primarily stabilizing, while shear thinning of the fluid tends to destabilize the fluid flow. In order to investigate the mechanisms involved, we perform an energy analysis of the flow under long-wave disturbances indicating that the convection of stress-gradient disturbances provides an additional viscoelastic mechanism for the destabilization of the flow, in contrast to the base state stress gradients which contribute to stabilization of the flow. Besides the usual long-wave instability, conditions are identified which lead to unstable disturbances of wavelength equal or smaller than the wavelength of the substrate. Experimental observations for Newtonian liquids have indicated that these short-wave instabilities will dominate and a similar behavior is predicted for viscoelastic liquids. Sometimes, before the short-wave instabilities, a hysteresis loop in the steady flow can be identified, which leads to a sharp change in the critical frequency. Finally, we examine the stability of the flow when subjected to disturbances in the spanwise direction and show that for highly elastic liquids 3D instabilities may arise.

DOI: [10.1103/PhysRevFluids.4.083304](https://doi.org/10.1103/PhysRevFluids.4.083304)

I. INTRODUCTION

A typical characteristic of film flows, either Newtonian or non-Newtonian, is the appearance of wavy interfacial instabilities which can be enhanced or mitigated by the presence of the substrate structure. Such instabilities may enhance the heat or mass transfer in cooling or mixing applications [1,2] whereas in coating applications wave instabilities may significantly affect the final product, reducing its quality. In the latter applications, though, an important factor is the rheology of the fluids involved: coating liquids are typically polymeric solutions which exhibit viscoelastic properties. In

*tsamo@chemeng.upatras.gr

Part I of this work (Pettas *et al.* [3], hereinafter referred to as Part I) we examined the steady flow of a viscoelastic liquid film over sinusoidal corrugations. We considered steady solutions which exhibit a periodicity identical to the periodicity of the substrate topography and investigated in detail the effects of both the geometrical characteristics of the substrate and the rheological parameters which characterize the flow behavior. The goal of this part of our study is to investigate the effect of viscoelasticity on the stability of films flowing over an undulated topography, analyzing in depth the interplay of elasticity along with the flow inertia and capillarity on the stability of films.

Early efforts to investigate the flow instabilities of a film over a flat substrate were reported by Benjamin [4] and Yih [5] who investigated the stability of a Newtonian film flowing over an inclined flat surface. They showed that the flow becomes unstable to long-wave disturbances above a critical value of the flow rate which depends on the angle of inclination, while for vertical substrates the flow is unstable even under creeping flow conditions. Subsequent studies examined various aspects of the flow stability in both the linear and nonlinear regimes [6], while some works considered the effect of surfactants [7,8]. Regarding the flow over structured surfaces, it was shown by Kalliadasis and Homsy [9] that the flow over isolated shallow rectangular topographies is stable for a wide range of the relevant parameters. Shortly after, Bielarz and Kalliadasis [10] performed time-dependent simulations, using lubrication theory for both two- and three-dimensional (2D and 3D) thin film flows over an isolated topography. They found that the free surface is stable against finite disturbances of the same wavelength as the topography even for finite values of the Reynolds number. These results were also supported by the experimental work of Vlachogiannis and Bontozoglou [11] and Argyriadi *et al.* [12] who studied the flow of a Newtonian liquid over rectangular trenches. Their experiments revealed that the critical flow rate for the onset of the instability is shifted to larger values as the steepness of the substrate increases, in the limit of small amplitude disturbances. D'Alessio *et al.* [13] considered the effect of the surface tension and topography steepness on the stability of a laminar film flow along an uneven surface. They observed that, under strong surface tension, the substrate corrugations could destabilize the flow of a Newtonian fluid, provided that the wavelength of the topography is sufficiently short compared to the film thickness. More recently, Heining and Aksel [14] predicted that the case of shallow films flowing along deep sinusoidal corrugations might lead to stabilization of the film flow and/or to unstable isles in the linear stability maps. Motivated by the previous results, Pollak and Aksel [15] reported experiments which have validated the existence of the unstable isles. Later on, Trifonov [16], by performing direct Navier-Stokes simulations combined with Floquet theory, validated these isles theoretically. Around that time, Cao *et al.* [17] provided evidence that, besides the long-wave instability that has been seen in previous studies, a short-wave mode may also arise in flows over deep periodic corrugations. They found that, with increasing inclination, the flow instability becomes short wave and, as a result, it has an intrinsic frequency which is insensitive to external excitation. Very recently, an attempt to summarize all the above results was made by Schörner *et al.* [18] through the presentation of stability maps (comparing experimental observations and theoretical predictions) in the parameter space of the inclination angle, viscosity and corrugation amplitude and wavelength of the topography. The linear stability analysis performed by these authors also confirmed the existence of short-wave instabilities under specific values of the flow rate reported by Cao *et al.* [17]. Up to now, Schörner and Aksel [19] have identified six characteristic stability map patterns that unify the linear instability of Newtonian films flowing over undulated inclines, reporting that the flow stability follows a universal pathway, which they called the "stability cycle."

All the aforementioned studies considered Newtonian liquid films. The flow of liquids following a generalized Newtonian law has been examined employing the Carreau model or a modified power law model by Millet *et al.* [20] and Ruyer-Quil *et al.* [21], respectively, for flat substrates. Furthermore, Heining and Aksel [14] considered the flow of a shear-thinning liquid over an inclined corrugated surface. All these works reported that shear thinning promotes flow instabilities, while the effect of shear thickening actually stabilizes the flow; an experimental confirmation of this behavior was provided by Allouche *et al.* [22].

As it was mentioned above, in many applications the flowing material is often a polymeric solution or a suspension of particles which exhibit viscoelastic properties. Up to now, the examination of the stability of viscoelastic films has been restricted to flows over flat inclined solid surfaces. In particular, asymptotic long-wave linear stability analysis has been carried out for flow over an inclined plane either assuming a second-order fluid [23] or an Oldroyd-B fluid [24,25]. As shown in these studies, the linear stability analysis for these two fluids yields precisely the same result and shows that there is a specific threshold of fluid elasticity, above which the fluid flow becomes unstable at zero inertia for a non-vertical inclination angle. There is, therefore, a purely elastic mechanism for the instability. However, according to Shaqfeh *et al.* [26], the growth rates of the resulting purely elastic waves are relatively small, and so the instability may be difficult to observe experimentally [27]. To the best of our knowledge, regarding the flow over structured surfaces, the only work that considers the stability of a viscoelastic film was presented by Dávalos-Orozco [28] for an Oldroyd-B liquid over a shallow wavy wall, under the long-wave assumption. As discussed in this study, even though fluid viscoelasticity has a destabilizing effect, the spatial resonance effect of the free surface with the wavy wall may conditionally lead to stabilization.

The goal of the present study is to examine the stability of viscoelastic films flowing over surfaces with sinusoidal corrugations of arbitrary depth. To this end, we will consider a viscoelastic liquid that follows the exponential Phan-Thien–Tanner (ePTT) constitutive law which allows a realistic variation of the shear and extensional fluid viscosities with the local rate of strain components as encountered in typical polymeric solutions. We will perform a linear stability analysis, employing the Floquet-Bloch theory and assuming that the steady solution which has been derived in Part I is subjected both to 2D and 3D disturbances of an arbitrary wavelength.

This paper is organized as follows: In Sec. II, the problem formulation along with the governing equations are given, and the numerical implementation is described in Sec. III. In Sec. IV, we proceed with the validation of our model against both numerical and experimental results found in the literature, while the discussion of the results from our numerical simulations is presented in Sec. V. Conclusions are drawn in Sec. VI.

II. PROBLEM FORMULATION

We consider the same physical system as in Part I, in which a viscoelastic liquid film flows under the effect of gravity along an inclined sinusoidally corrugated substrate normal to the main flow direction (see Fig. 1 in Part I). We use the same model, the same notation, and the same scalings under which the following dimensionless numbers arise: the Reynolds number Re , Stokes number St , Kapitza number Ka , Weissenberg number Wi , viscosity ratio β , and inclination angle α . For the definitions of all dimensionless groups the reader is referred to Table I of Part I.

A. Governing equations

The flow is governed by the momentum and mass conservation equations, which under the arbitrary Eulerian-Lagrangian (ALE) formulation in dimensionless form are given by

$$Re \left(\frac{\partial \mathbf{u}}{\partial t} + (\mathbf{u} - \mathbf{u}_m) \cdot \nabla \mathbf{u} \right) + \nabla P - \nabla \cdot \boldsymbol{\tau} - St \mathbf{g} = 0, \quad (1)$$

$$\nabla \cdot \mathbf{u} = 0, \quad (2)$$

where $\mathbf{u} = (u_x, u_y, u_z)^T$, P , and $\boldsymbol{\tau}$, denote the velocity, pressure, and stress fields, respectively, $\nabla = (\partial_x, \partial_y, \partial_z)^T$ denotes the gradient operator for Cartesian coordinates, and $\mathbf{u}_m = \partial x / \partial t$ the velocity of the mesh nodes in the flow domain. We also define the unit gravity vector as $\mathbf{g} = (\sin \alpha, -\cos \alpha, 0)^T$,

The extra stress tensor, $\boldsymbol{\tau}$, is split into a purely Newtonian part $2\beta \dot{\boldsymbol{\gamma}}$ and a polymeric contribution $\boldsymbol{\tau}_p$:

$$\boldsymbol{\tau} = 2\beta \dot{\boldsymbol{\gamma}} + \boldsymbol{\tau}_p, \quad (3)$$

where $\dot{\boldsymbol{\gamma}} = \frac{1}{2}(\nabla \mathbf{u} + \nabla \mathbf{u}^T)$ is the rate of strain.

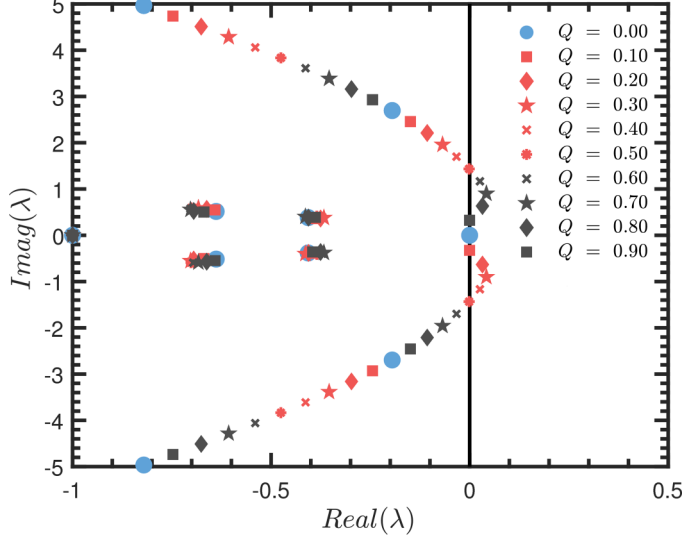


FIG. 1. Eigenspectrum for $Re = 8$; the flowing liquid is *Elbesil 65* (see Table I), for $Q \in [0, 1)$. The light blue dots indicate the eigenvalues which have been calculated for $Q = 0$; the light red symbols indicate the eigenvalues for Q in the range $(0, 0.5]$ and gray symbols indicate the eigenvalues for Q in the range $(0.5, 1]$.

To account for the viscoelasticity of the material we use the affine exponential form of the Phan-Thien and Tanner model [29]:

$$Y(\boldsymbol{\tau}_p)\boldsymbol{\tau}_p + Wi \overset{\nabla}{\boldsymbol{\tau}}_p - 2(1 - \beta)\dot{\boldsymbol{\gamma}} = 0, \quad Y(\boldsymbol{\tau}_p) = \exp\left(\frac{\varepsilon}{1 - \beta} Wi \text{trace}(\boldsymbol{\tau}_p)\right), \quad (4)$$

where $\overset{\nabla}{\boldsymbol{\tau}}_p = \frac{\partial \boldsymbol{\tau}_p}{\partial t} + (\mathbf{u} - \mathbf{u}_m) \cdot \nabla \boldsymbol{\tau}_p - \boldsymbol{\tau}_p \cdot \nabla \mathbf{u} - (\boldsymbol{\tau}_p \cdot \nabla \mathbf{u})^T$ is the upper convective derivative of $\boldsymbol{\tau}_p$. The viscoelastic fluid properties depend on the dimensionless parameters Wi , β , and ε ; the physical relevance of these parameters is briefly discussed in Part I.

B. Boundary conditions

Along the air-liquid interface we apply the following interfacial stress balance:

$$\mathbf{n} \cdot (-P\mathbf{I} + \boldsymbol{\tau}) = \frac{\kappa}{Ca} \mathbf{n}, \quad (5)$$

where \mathbf{n} is the outward unit vector normal to the free surface and κ is the mean curvature defined as

$$\kappa = -\nabla_s \cdot \mathbf{n}, \quad \nabla_s = (\mathbf{I} - \mathbf{nn}) \cdot \nabla. \quad (6)$$

TABLE I. Material properties and dimensionless quantities of liquids used in this paper.

Notation	Viscosity (mPa s)	Density ($\frac{\text{kg}}{\text{m}^3}$)	Surface tension ($\frac{\text{mN}}{\text{m}}$)	Kapitza number	Dimensionless unit cell length $L = \frac{L^*}{l_c^*}$	Geometric aspect ratio A/L
<i>Elbesil 65</i>	62.40	958.5	19.91	3.75	13.765	0.40
<i>Elbesil 100</i>	96.6	963.2	20.07	2.09	13.765	0.40
<i>Elbesil 145</i>	139.1	964.8	20.01	1.28	13.765	0.40
68% w/w aqueous glycerol	12.8	1170	68.83	110	4.9	0.167

In Eq. (5) the ambient pressure has been set equal to zero (datum pressure) without loss of generality. Along the free surface, we also impose the kinematic condition

$$\mathbf{n} \cdot \left(\mathbf{u} - \frac{\partial \mathbf{x}}{\partial t} \right) = 0, \quad (7)$$

while, along the walls of the substrate, we impose the usual no-slip, no-penetration boundary conditions. Additionally, we impose periodic boundary conditions in the velocity and stress field between the inflow and the outflow of the domain. As noted in Part I, we assume that the steady flow has the same periodicity as the substrate structure (i.e., we assume that the steady solution is L -periodic):

$$\mathbf{u}|_{x=0} = \mathbf{u}|_{x=L}, \quad (8)$$

$$\mathbf{n} \cdot (-\mathbf{PI} + \boldsymbol{\tau})|_{x=0} = \mathbf{n} \cdot (-\mathbf{PI} + \boldsymbol{\tau})|_{x=L}. \quad (9)$$

Finally, the film height at the entrance of the unit cell, H^* , is determined by requiring that the dimensionless flow rate is equal to unity:

$$q = \int_0^{H^*/H_N^*} u_x dy = 1. \quad (10)$$

In Table I, we present the material properties and the geometric characteristics used in the simulations of this paper. As a base case, we choose the Newtonian properties of *Elbesil 65* ($Ka = 3.75$) flowing over a substrate with $L^* = 20$ mm and $A^* = 8$ mm. This is a setup which has frequently been used in experiments [18,19]. Throughout the paper the dimensional and dimensionless geometric characteristics are constant such that, $L = 13.765$, $A/L = 0.4$; an exception of that is Fig. 4 where for validation purposes we use different geometric characteristics; see Table I for 68% w/w water glycerol. Moreover, the inclination angle is set at $\alpha = 10^\circ$ and, unless stated otherwise, the parameters Ka and β are set at 3.75 and 0.1, respectively.

III. NUMERICAL IMPLEMENTATION

The base flow is steady, two-dimensional, and is assumed to be L -periodic, the characteristics of which were discussed in detail in Part I. We consider the stability of this steady flow subjected to infinitesimal 2D and 3D perturbations. To this end, we map the perturbed physical domain (x, y, z) to a known reference domain (η, ξ, ζ) . The variables are written in the computational domain and are decomposed into a part which corresponds to the base state solution and an infinitesimal disturbance using the following ansatz:

$$\begin{bmatrix} \mathbf{u} \\ P \\ \mathbf{G} \\ \boldsymbol{\tau}_p \end{bmatrix} (\eta, \xi, \zeta, t) = \begin{bmatrix} \mathbf{u}_b \\ P_b \\ \mathbf{G}_b \\ \boldsymbol{\tau}_{p,b} \end{bmatrix} (\eta, \xi) + \delta \begin{bmatrix} \mathbf{u}_d \\ P_d \\ \mathbf{G}_d \\ \boldsymbol{\tau}_{p,d} \end{bmatrix} (\eta, \xi, \zeta, t), \quad (11)$$

$$\begin{bmatrix} x \\ y \\ z \end{bmatrix} (\eta, \xi, \zeta, t) = \begin{bmatrix} x_b \\ y_b \\ \zeta \end{bmatrix} (\eta, \xi) + \delta \begin{bmatrix} x_d \\ y_d \\ 0 \end{bmatrix} (\eta, \xi, \zeta, t). \quad (12)$$

The first terms on the right-hand side of these equations represent the base solution, indicated by the subscript b , while the second ones are the perturbation, indicated by the subscript d while $\delta \ll 1$. Introducing Eqs. (11) and (12) in the weak form of the governing equations, we derive a

linearized set of equations for the flow in the bulk and the corresponding boundary conditions; a detailed description is provided in Appendix A.

The disturbances are represented by a set of normal modes as follows:

$$\begin{bmatrix} \mathbf{u}_d \\ P_d \\ \mathbf{G}_d \\ \boldsymbol{\tau}_{p,d} \\ \mathbf{x}_d \end{bmatrix} (\eta, \xi, \zeta, t) = \begin{bmatrix} \mathbf{u}'_d \\ P'_d \\ \mathbf{G}'_d \\ \boldsymbol{\tau}'_{p,d} \\ \mathbf{x}'_d \end{bmatrix} (\eta, \xi, \zeta) e^{\lambda t + ikz}, \quad (13)$$

where \mathbf{x}_d is the disturbance of the position vector [$\mathbf{x}_d = (x_d, y_d, 0)^T$]. According to our ansatz, an exponential dependence on time is assumed; here λ denotes the growth rate. If the calculated λ turns out to have a positive real part, the disturbance grows with time, and therefore the corresponding steady state is unstable. The disturbances $\mathbf{u}'_d, P'_d, \mathbf{G}'_d, \boldsymbol{\tau}'_{p,d}, \mathbf{x}'_d$ are discretized employing finite element basis functions in the streamwise and spanwise directions while Fourier modes are employed in the transverse ζ direction; k denotes the wave number of the perturbation in the z direction. A detailed description is provided in Appendix A.

A. Periodic boundary conditions and implementation of Floquet-Bloch theory

For flows over periodic structured surfaces, the most unstable disturbance for the specific system may have a wavelength that exceeds the period of the domain. Thus, it becomes evident that if one assumes periodic conditions for the disturbances between the inflow and outflow boundaries, the overall linear stability of the system cannot be captured unless a sufficiently long computational domain is considered. This would imply a formidable computational cost in the case where long-wave disturbances are the most unstable ones as is typical for thin film flows. As we will discuss below, the most appropriate and efficient way to deal with this issue is to employ the Floquet-Bloch theory, which allows us to model the flow over a structured surface by considering the small periodic domain of the topography, thus maintaining a considerably reduced computational cost, while examining disturbances with wavelengths that may extend over multiple trenches or fractions thereof.

According to Bloch's theorem [30], it is sufficient to look for solutions such that the disturbances between the inflow and outflow of the unit cell are related to each other with the following expression:

$$\begin{bmatrix} \mathbf{u}'_d \\ P'_d \\ \mathbf{G}'_d \\ \boldsymbol{\tau}'_{p,d} \\ y'_d \end{bmatrix} \Big|_{x=L} = \begin{bmatrix} \mathbf{u}'_d \\ P'_d \\ \mathbf{G}'_d \\ \boldsymbol{\tau}'_{p,d} \\ y'_d \end{bmatrix} \Big|_{x=0} e^{2\pi Q i}. \quad (14)$$

Using this formulation, the unknown disturbances, $(\mathbf{u}'_d, P'_d, \mathbf{G}'_d, \boldsymbol{\tau}'_{p,d}, y'_d)^T$, will be determined by imposing Eq. (14) at the edges of the periodic domain, which enforces that, for finite real values of Q , the disturbances will not be L -periodic. For example, when $Q = 0.5$ the imposed perturbation has a wavelength that is twice the size of the physical domain, whereas $Q \rightarrow 0$ corresponds to disturbances with wavelength much larger than the size of the periodic domain. Disturbances with $Q = 0$ should be distinguished, since in that case Eq. (14) reduces to typical periodic boundary conditions, and thus the case corresponds to disturbances that have the same period or aliquots of the basic solution, i.e., correspond to superharmonic instabilities.

B. The Arnoldi algorithm

After we discretize the linearized set of equations, we end up with a generalized eigenvalue problem of the form

$$\mathbf{A}\mathbf{w} = \lambda\mathbf{M}\mathbf{w}, \quad (15)$$

where \mathbf{A} and \mathbf{M} are the Jacobian and the mass matrix respectively, with λ the eigenvalues and \mathbf{w} the corresponding eigenvectors. This eigenvalue problem is solved using Arnoldi's method [31–36] which allows us to locate only the eigenvalues of interest; for determining critical conditions, we need those eigenvalues with the smallest real part. According to our framework, the solution is stable if the real parts of all eigenvalues are less than or equal to zero for all values of Q .

To implement Arnoldi's algorithm, we use the public domain code ARPACK [36] which computes the eigenvalues with the largest magnitude. Since we are interested only in the eigenvalues with the smallest real part, and to avoid the singularity of the mass matrix, the following shift-and-invert transformation is employed:

$$\mathbf{K}\mathbf{w} = \nu\mathbf{w}, \quad \text{where } \mathbf{K} = (\mathbf{A} - \lambda\mathbf{M})^{-1}\mathbf{M} \quad \text{and} \quad \nu = \frac{1}{\lambda - s}. \quad (16)$$

The leading eigenvalues of the above system are those eigenvalues of the original problem that are closest to the complex shift value, s ; when ν is maximum, then $\lambda - s$ is minimum. Therefore, with a sequence of such complex shifts, adaptively generated with a procedure similar to the one described in [32–35], it is possible to obtain the desired part of the eigenspectrum (i.e., the leading eigenvalues with the smallest real part). The accuracy of the converged eigenpairs is independently checked by evaluating the residual $|\mathbf{A}\mathbf{w} - \lambda\mathbf{M}\mathbf{w}|$, and this quantity is always less than 10^{-12} for the reported results.

C. Evaluation of the eigenspectrum and neutral stability curves

In Fig. 1 we present a typical eigenspectrum for a Newtonian liquid flowing over a sinusoidal topography. This spectrum is produced by solving the eigenvalue problem for different values of Q in the range $[0, 1)$. For $Q \neq 0, 0.5$ the Jacobian matrix has complex entries [see Eq. (14)], and therefore the calculated eigenvalues do not appear in conjugate pairs. However, the continuous spectrum which is recovered by evaluating the eigenvalues for all values of Q in the range $[0, 1)$ appears to be fully symmetric with respect to the axis of $\text{Real}(\lambda)$. For instance, we notice that the calculated eigenvalues for $Q = 0.7$ are the conjugate eigenvalues of the spectrum for $Q = 0.3$; see Fig. 1. As a result, it is possible to calculate the total spectrum by considering the values of the Bloch wave number Q simply in the range of $[0, 0.5]$ instead of $[0, 1)$. The flow will be considered to become unstable for a specific value of Re when for any value of Q in the range of $[0, 0.5]$ there exists at least one eigenvalue with positive real part. Neutral conditions will arise when the real part of the most dangerous eigenvalue becomes equal to zero.

After a critical point has been detected for some combination of Re and Q (i.e., the real part of the most critical eigenvalue is close to zero) it is desirable to locate it precisely and to trace its path in order to obtain the dependence of the critical Reynolds number as a function of the Bloch wave number Q for fixed geometrical characteristics of the substrate, liquid properties, and inclination angle. To this end, we employ an algorithm similar to the one proposed by Hackler *et al.* [37], and for every value of Q we solve the following coupled set of equations:

$$\mathbf{R}(\mathbf{v}; \text{Re}) = 0, \quad (17)$$

$$(\mathbf{A} - \lambda\mathbf{M})\mathbf{w} = 0, \quad (18)$$

$$\mathbf{w}_{\text{trial}} \cdot \mathbf{w} = 1, \quad (19)$$

$$\text{Real}(\lambda) = 0. \quad (20)$$

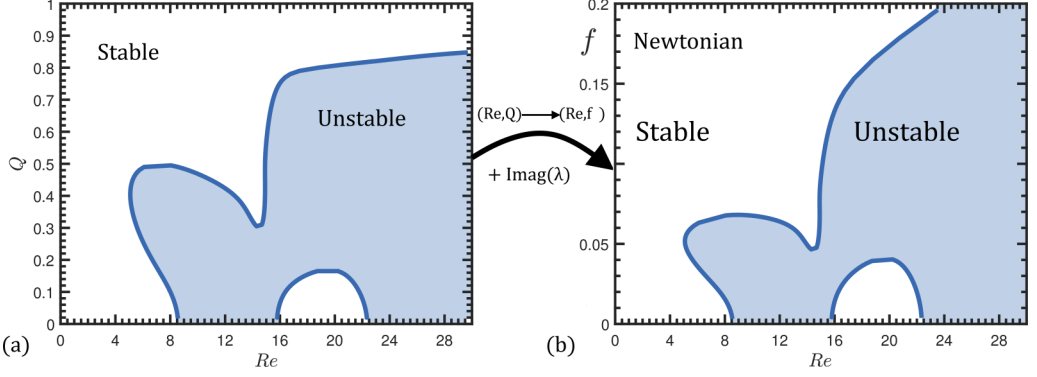


FIG. 2. Stability map for the *Elbesil 65* (see Table I), in (a) the Floquet parameter space (Re , Q) and in (b) the frequency space (Re , f). The light blue area indicates the unstable regimes of the fluid flow.

Equation (17) represents the set of equations for the steady state flow for the vector of unknowns \mathbf{v} (velocities, pressures, stresses, velocity gradients, and node positions) as a function of Re . Equation (18) is the eigenvalue problem for the specific value of Q . Equation (19) is the normalizing condition for the eigenvector, and Eq. (20) the condition that the growth rate of the eigenvalue vanishes. First, we solve Eq. (17) to determine the steady solution and Eq. (18) to detect the eigenvalue to be tracked (i.e., the eigenvalue with the largest growth rate) for a specific value of Re and the Floquet parameter Q . The latter are introduced as an initial guess to the system of equations (17)–(20). As $\mathbf{w}_{\text{trial}}$ we choose the eigenvector of the corresponding eigenvalue. The system is solved iteratively until the real part of the eigenvalue followed becomes smaller than 10^{-8} . After the algorithm converges, we increase Q to $Q + dQ$ and use the calculated steady state, eigenvector, and critical eigenvalue of Q as the initial condition for the new iteration at $Q + dQ$. Given a good initial guess, this algorithm ultimately converges quadratically even if the path of the steady state is close to a hysteresis loop. The implementation of this tracking algorithm is described in Appendix B.

We use this algorithm to produce the stability map of *Elbesil 65* (see Table I) in the (Re , Q) plane shown in Fig. 2(a). In this figure, the neutral stability curve is indicated with the continuous blue line, while the white and light blue areas represent the stable and the unstable regimes, respectively. As shown in this figure for disturbances with infinite wavelength ($Q \rightarrow 0$, $Q > 0$) the critical Re_c is calculated to be 8.51. Figure 2(a) presents the stability characteristics of the flow for different values of Re as a function of Q , which is associated with the wavelength of the imposed disturbance. Examining all wavelengths, the flow becomes first unstable for $Q = 0.405$, where the critical $Re_c = 5.09$. In experiments, instead of imposing a disturbance with a specific wavelength, it is easier to impose a disturbance with a specific frequency. According to our formulation, the imaginary part of the eigenvalue corresponds to the dimensionless frequency of the disturbance and can be related to the dimensional frequency of the disturbances using the following expression:

$$f^* = \frac{\text{Imag}(\lambda) U_N^*}{2\pi H_N^*} = \frac{\text{Imag}(\lambda)}{2\pi} Re^{1/3} St^{-2/3} \left(\frac{\mu^*}{\rho^* g^{*2}} \right)^{-1/3}. \quad (21)$$

By scaling the dimensional frequency with the viscous timescale $t_v^* = (\frac{\mu^*}{\rho^* g^{*2}})^{1/3}$, so that the timescale is independent of Re , the dimensionless frequency is given by the following expression:

$$f = \frac{\text{Imag}(\lambda)}{2\pi} Re^{1/3} St^{-2/3}. \quad (22)$$

Based on this definition, it is possible to present the same stability map shown in Fig. 2(a) in the (Re , f) plane; see Fig. 2(b). The two representations are interchangeable while the latter has the

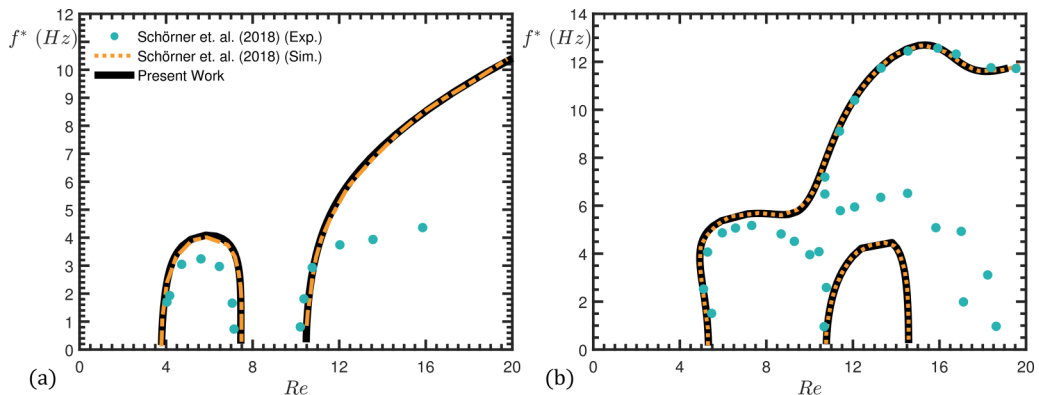


FIG. 3. Comparison of the predicted neutral curves for Newtonian liquids with previous studies. The liquids used are (a) *Elbesil 145* and (b) *Elbesil 100*; see Table I. Experimental data are shown with dots while the theoretical predictions are presented with lines; the continuous black line and orange dashed line refer to the current work and Schörner *et al.* [18], respectively.

advantage that the theoretical predictions can be directly compared with experimental observations [38]. For the rest of the discussion, we will follow the latter representation of our numerical results.

IV. VALIDATION

Before we proceed with the discussion of our results, we present a series of validation tests of our in-house code with experimental observations and theoretical predictions for relevant flows that can be found in the literature. First, we have examined the stability of Newtonian films over corrugated surfaces subjected to 2D disturbances ($k = 0$), and we present in Fig. 3 the theoretical and experimental data for two different liquids, *Elbesil 100* and *Elbesil 145*, the properties of which are given in Table I.

In Fig. 3, we depict the dependence of the critical Re_c on the frequency of the instability. Our results are in very good agreement with both the theoretical curves and the experimental data, [18]. Note that the linear stability analysis predicts the existence of both a neutral curve for $Re > 10.5$ as well as an unstable isle for $3.9 < Re < 7.8$ [see Fig. 3(a)], the nature of which will be described later in the paper. Interestingly, in between those two regions, the substrate corrugations provoke a narrow window where all linear perturbations are damped, i.e., for $7.8 < Re < 10.5$. Above a specific value of Re , the experimental observations deviate from the theoretical results and the deviation is larger at the higher viscosity liquids for $Re > 12$; see Fig. 3. Since there is no guarantee that all base flow formations in the experiment correspond to the steady state solution theory, it is possible thick films may have different flow arrangement (i.e., the L -periodicity of the fluid flow may have broken down). This hypothesis is also supported by the study of Tseluiko *et al.* [39] who found that the film flow might experience a sequence of multiple steady states which in general have a different periodicity than the wall. However, finding and analyzing this type of bifurcation is outside the scope of this study.

Cao *et al.* [17] performed experiments for an aqueous-glycerol liquid (68% w/w, see Table I) flowing over a sinusoidal substrate with $L^* = 12$ mm and $A^* = 2$ mm. In Fig. 4 we present the value Re_c/Re_{flat} , where $Re_{\text{flat}} = \frac{5}{6} \cot \alpha$, as a function of the inclination angle. Along the continuous blue line, the Bloch wave number varies from $Q = 0.15$ at $a = 2^\circ$ to $Q = 0.81$ at $a = 45^\circ$. For all values of the inclination angle, there is good agreement with the experiments [17] in terms of the value of the critical Re number. However, it is important to note that even though our theoretical calculations predict that for all inclination angles the most unstable modes are long-wave disturbances, Cao *et al.* [17] observed instead the appearance of short-wave instabilities for large values of the inclination

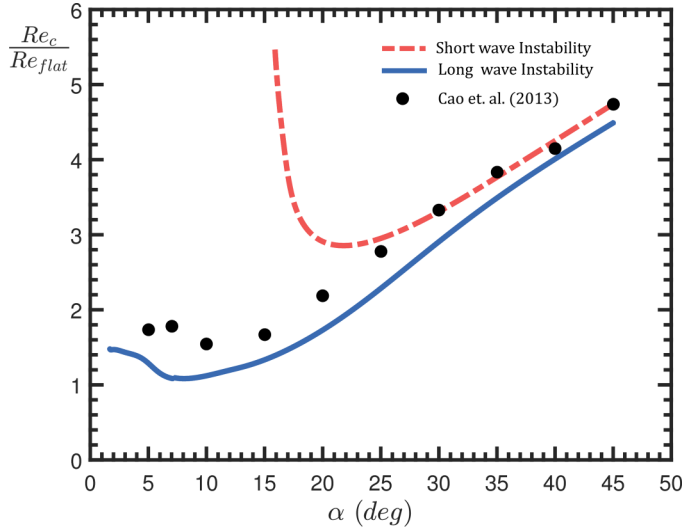


FIG. 4. Comparison of the predictions of this study with the experimental data of Cao *et al.* [17] as a function of inclination angle. Black dots depict the experiments; the continuous blue line indicates the critical Reynolds number with the minimum value for finite values of Q , and the dashed red line indicates the most unstable mode for $Q = 0$. The Kapitza number is 110, whereas the geometric parameters are $L = 4.9$, $A/L = 0.167$.

angle ($a \geq 25^\circ$). For instance, for inclination angle $a = 30^\circ$ we predict that the most unstable mode corresponds to a disturbance with $Q = 0.73$ and frequency $f^* = 12.84$ Hz, whereas Cao *et al.* [17] observed instability with a frequency of 19.35 Hz. As shown in Fig. 4, according to our predictions the second most unstable mode is a short-wave instability which corresponds to $Q = 0$ and frequency $f^* = 18.68$ Hz, which is very close to the experimental observations. Although this mode becomes unstable at slightly higher values of Reynolds number than in the experiments, the difference becomes very small for inclination angles $a \geq 25^\circ$, which can explain why this mode has been observed.

To build further confidence we have also compared the predictions of our model with theoretical predictions in the literature for the case of a viscoelastic film flow over an inclined flat solid surface. Figure 5(a) presents the predictions of our model for a steady flow subjected to 2D disturbances ($k = 0$) for different values of ε and for $\beta = 0.1$. In the limit of the Oldroyd-B model (ePTT for $\varepsilon = 0$) we find an excellent agreement between our numerical results and the analytical expression of Lai [25]:

$$\text{Re}_c = \frac{5}{6} \cot a - \frac{5}{2} \text{Wi}(1 - \beta). \quad (23)$$

This analytical expression describes that, except for the inertia, the viscoelastic films over flat plates have a second destabilizing effect due to fluid elasticity. Interestingly, Eq. (23) describes that there is a specific value of Wi for which the instability arises in the absence of inertia. Nevertheless, for nonzero values of ε , a liquid following the ePTT law expresses shear thinning; with increasing ε the effect of shear thinning increases. As shown in Fig 5(a), shear thinning appears to destabilize further the flow monotonically. This is in agreement with predictions regarding the stability of generalized Newtonian liquids [21,22]. Finally, as depicted in Fig. 5(b), our code accurately predicts the critical conditions when the flow is subjected to disturbances in the spanwise direction; here we compare our predictions with the analytical expression provided by Kang and Chen [24] which has

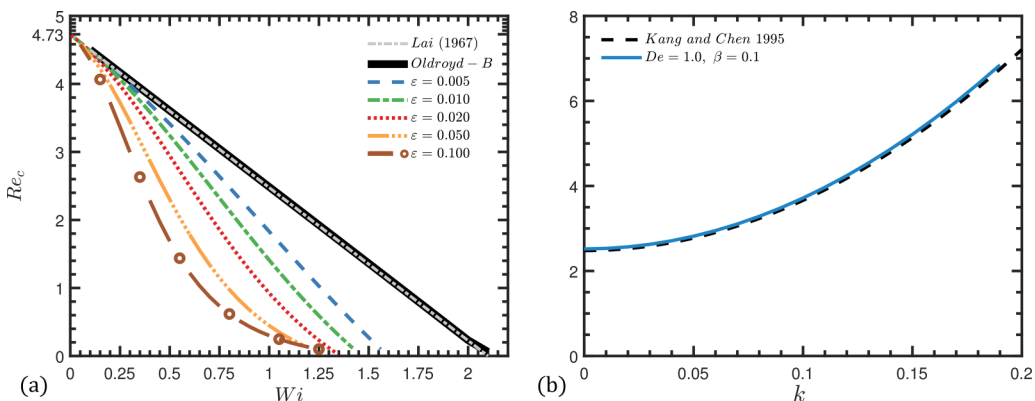


FIG. 5. (a) Critical Reynolds number for the Nusselt flow of a viscoelastic liquid subjected to 2D disturbances. The gray dashed line is the analytical expression derived by Lai [25] using the Oldroyd-B model with $\beta = 0.1$. The rest of the lines correspond to our neutral curves for long-wave disturbances ($Q = 10^{-2}$) and different ε values. (b) Critical Reynolds number for the Nusselt flow of a viscoelastic liquid subjected to 3D disturbances as a function of k . Comparison with the analytical expression by Kang and Chen [24] for $Ka = 10, L = 100$.

been modified to account for 3D disturbances, following the arguments described by Benjamin [40]:

$$\text{Re} - \frac{5}{6} \cot a \left(1 + \left(\frac{k}{k_{2D}} \right)^2 \right) + \frac{5}{6} k_{2D}^2 \left(1 + \left(\frac{k}{k_{2D}} \right)^2 \right) Ka \left(\frac{1}{\sin a (3\text{Re})^2} \right)^{\frac{1}{3}} - \frac{5}{2} \text{Wi} (1 - \beta) = 0, \quad (24)$$

where k denotes the wave number in the spanwise direction and $k_{2D} = \frac{2\pi Q}{L}$.

V. RESULTS AND DISCUSSION

A. Linear stability analysis for the Oldroyd-B fluid

We will now turn our attention to the stability of the steady flow described above. We will first focus on 2D disturbances to an Oldroyd-B fluid and then proceed with the investigation of the stability of an ePTT fluid, including 3D disturbances.

1. Effect of long-wave disturbances

We begin our discussion by examining the stability of the steady flow when subjected to long-wave 2D disturbances. To this end, we focus on disturbances with Bloch wave number $Q = 10^{-2}$. In Fig. 6, the growth rate of the most unstable eigenvalue is presented as a function of Re . As expected, for both Newtonian and viscoelastic liquids the flow is found to be stable for low values of Re and unstable as Re assumes large values. At intermediate values of Re , though, the growth rate of the most unstable mode exhibits a nonmonotonic behavior. In the case of the Newtonian liquid, the flow first becomes unstable at $Re = 8.52$ while the maximum growth rate was calculated at $Re = 14.77$, which coincides with the point of resonance of the steady free surface with the bottom wall [see Fig. 4(a) in Part I]. With further increase of Re , the flow becomes stable in the range $16 \leq Re \leq 22.1$. For higher values of Re , the steady shape of the interface becomes almost flat, and the flow is destabilized by inertia similarly to Nusselt flow, over a flat substrate, although there $Re_c = \frac{5}{6} \cot \alpha = 4.73$.

In the case of the viscoelastic liquid, the maximum growth rate arises at $Re = 16.25$, which coincides with the resonance point of the steady free surface with the bottom wall [see Fig. 4(a) in Part I]. Additionally, an isle of stability also arises for higher values of Re ($17.39 \leq Re \leq 21.78$)

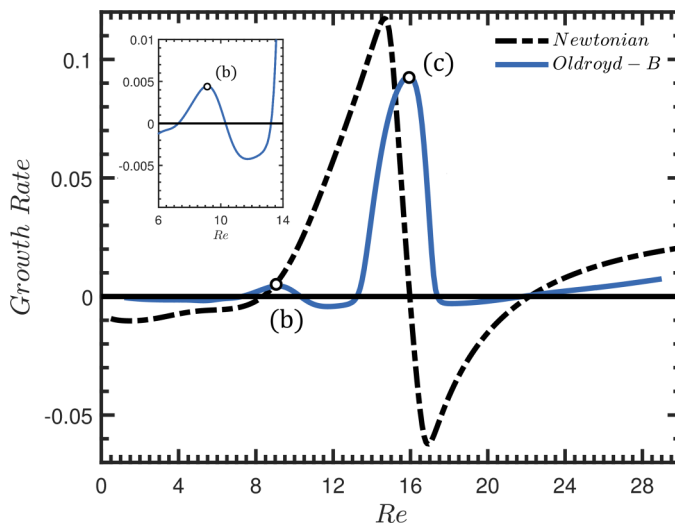


FIG. 6. The growth rate of the most unstable eigenvalue for an Oldroyd-B (continuous blue line) and a Newtonian (dashed black line) liquid over a sinusoidal topography. The remaining parameters are $Wi = 1$, $\varepsilon = 0$.

although the size of this region is significantly smaller than its Newtonian counterpart. Interestingly, a second instability region emerges for $7.26 \leq Re \leq 10.31$, albeit with smaller maximum growth rate. The position of this peak coincides with the position of the change in slope that is seen in Fig. 4(a) in Part I (i.e., for $Re \cong 9$) indicating that a weaker resonance exists in this range. In addition, we observe that an isle of stability arises between these two unstable regions, i.e., for $10.31 \leq Re \leq 13.22$.

Note that, in Fig. 6, due to the specific choice of Q ($Q = 10^{-2}$), the wavelength of the disturbance corresponds to 100 unit cells and cannot be presented in the paper. To appreciate the long-wavelength disturbance, in Fig. 7 we examine a slightly larger value of Q ($Q = 0.1$), where we present the steady state profile of the free surface along with the disturbance profile of the most unstable mode and their superposition over a complete wavelength (10 unit cells); the black dotted line depicts the long-wavelength disturbance, which in this case is constructed by connecting the extreme values inside each unit cell. The long-wavelength disturbance clearly is $\cos(2\pi \frac{x^*}{10L^*})$. Moreover, Figs. 7(a) and 7(b) depict the cases for $Re = 9.1$ and $Re = 16.25$, which correspond to positions of the two local maxima of the growth rate. In both cases, the disturbances are localized in the region of the cusp in the steady state solution, and therefore it can be deduced that the presence of the cusp has a destabilizing effect on the flow due to the intense velocity gradients and normal polymeric stresses ($\tau_{p,xx}$) that arise in that region.

2. Energy analysis for the flow of an Oldroyd-B liquid subjected to long-wave disturbances

To identify the physical mechanism that leads to the destabilization of the flow, we perform an energy analysis, which has been used successfully in the past for the analysis of various viscoelastic flows [33,34,41,42]. The energy method considers the interaction of the base flow and the disturbance flow by evaluating the mechanical energy balance for the perturbed system. Hence, it is used to determine the stabilizing and destabilizing effects of the coupling of the velocities and stresses of the base and disturbance flows. The method is described in detail in the Appendix of Karapetsas and Tsamopoulos [33].

The disturbance energy equation is obtained by taking the inner product of the linearized perturbation of the momentum equation with the perturbation velocity, and integrating the resulting

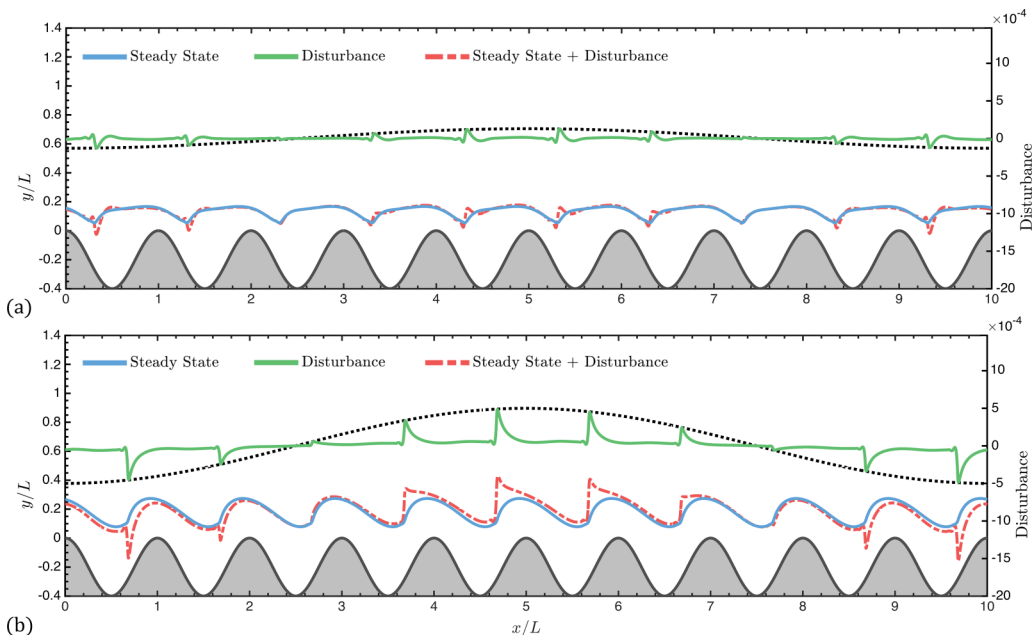


FIG. 7. Steady free surface (continuous blue line) and its corresponding long-wave disturbances for $Q = 0.1$ (continuous green line), calculated at (a) $Re = 9.1$, (b) $Re = 16.25$. The red dash-dotted line in (a) and (b) indicates the superposition of the steady free surface and the disturbance, where the magnitude of the latter has been magnified 500 times. The black dotted lines indicate the long-wave disturbances. The remaining parameters are $Wi = 1$, $\varepsilon = 0$.

equation over a complete wavelength of the disturbance with $0 < x < \frac{L}{Q}$ and one period in time (i.e., $0 < t < T = \frac{1}{f}$). After some manipulation the energy budget becomes

$$\text{Re} \left(\frac{dE_k}{dt} + \phi_{\text{Rey}} \right) = -\phi_{\text{pre}} + \phi_{\text{vis}} - \frac{dE_p}{dt} + \phi_p, \quad (25)$$

where $\phi_p = \phi_{pv1} + \phi_{ps1} + \phi_{pv2} + \phi_{ps2}$. The various terms of Eq. (25) and their physical interpretations are given in Table II. Note that for the evaluation of all terms shown in Eq. (25) we take just the real part of the perturbations, while the subscript b denotes the base state and d the disturbance variables.

In the presence of inertia, the term dE_k/dt , which signifies the rate of change of kinetic energy with time, can be used as the term which indicates the stability or instability of the flow. The term ϕ_{Rey} corresponds to the Reynolds stresses, ϕ_{pre} is the energy associated with the perturbation of the pressure, and ϕ_{vis} is the viscous dissipation energy term, which is always negative and thus has a stabilizing effect on the flow. Accounting for the viscoelasticity of the fluid, the term dE_p/dt describes the growth rate associated with the polymeric stresses, while the remaining terms denoted as ϕ_p are related to the coupling of the polymeric stresses with the velocity field.

The energy analysis was performed for a Newtonian and an Oldroyd-B liquid for $Wi = 1$ and $\beta = 0.1$ while varying the Reynolds number and assuming that the flow is subjected to long-wave disturbances, $Q = 10^{-2}$. The various terms of the energy equation for both cases are presented in Fig. 8, without the normalization of the eigenvectors. In the case of a Newtonian liquid [see Fig. 8(a)], we find that the only positive term is ϕ_{Rey} , while ϕ_{pre} becomes positive at supercritical conditions. Additionally, the term ϕ_{vis} is always negative since viscous dissipation stabilizes the flow. The term ϕ_{Rey} is always positive for low values of Re , while at the transition from stability

TABLE II. The physical interpretation of terms arising in the energy budget for an Oldroyd-B liquid.

Term	Physical interpretation
$\frac{dE_k}{dt} = \int_{V_t} \frac{d\mathbf{u}_d}{dt} \cdot \mathbf{u}_d dV dt$	The rate of change of the kinetic energy with time
$\frac{dE_p}{dt} = \int_{V_t} Wi \nabla \cdot \frac{\partial}{\partial t} \boldsymbol{\tau}_{p,d} \cdot \mathbf{u}_d dV dt$	Growth rate of polymeric stresses
$\phi_{\text{Rey}} = \int_{V_t} (\mathbf{u}_d \cdot \nabla \mathbf{u}_b + \mathbf{u}_b \cdot \nabla \mathbf{u}_d) \cdot \mathbf{u}_d dV dt$	Reynolds stresses
$\phi_{\text{pre}} = \int_{C_t} \mathbf{n} \cdot P_d \mathbf{I} \cdot \mathbf{u}_d dC dt$	Energy associated with the pressure perturbation
$\phi_{\text{vis}} = \int_{V_t} \nabla \cdot (\nabla \mathbf{u}_d + \nabla \mathbf{u}_d^T) \cdot \mathbf{u}_d dV dt$	Viscous dissipation energy term
$\phi_{pv1} = \int_{V_t} Wi \nabla \cdot (\mathbf{u}_d \cdot \nabla \boldsymbol{\tau}_{p,b}) \cdot \mathbf{u}_d dV dt$	Coupling of the base state stress gradients with the velocity perturbations
$\phi_{pv2} = \int_{V_t} Wi \nabla \cdot [\boldsymbol{\tau}_{p,b} \cdot \nabla \mathbf{u}_d + (\boldsymbol{\tau}_{p,b} \cdot \nabla \mathbf{u}_d)^T] \cdot \mathbf{u}_d dV dt$	Coupling of the velocity gradient perturbation with the base state stresses.
$\phi_{ps1} = \int_{V_t} Wi \nabla \cdot [\mathbf{u}_b \cdot \nabla \boldsymbol{\tau}_{p,d}] \cdot \mathbf{u}_d dV dt$	Coupling of the stress gradient perturbation with the base state velocity
$\phi_{ps2} = \int_{V_t} Wi [\boldsymbol{\tau}_{p,d} \cdot \nabla \mathbf{u}_b + (\boldsymbol{\tau}_{p,d} \cdot \nabla \mathbf{u}_b)^T] \cdot \mathbf{u}_d dV dt$	Coupling of the stress perturbation with the base state velocity gradient

to instability this term appears to increase rapidly, indicating that this term drives the instability in Newtonian liquids. This is not surprising, as it is well known that inertial effects drive this instability and ϕ_{Rey} is associated with the Reynolds stresses.

For a viscoelastic liquid, the mechanism of the instability is more complicated, as seen in Fig. 8(b); in this figure, we have omitted the term ϕ_{vis} since it is always stabilizing. Interestingly, in the case of the viscoelastic fluids besides the inertia terms, expressed by the term ϕ_{Rey} , we find that the terms ϕ_{ps1} and ϕ_{pv2} also acquire positive values contributing to the destabilization of the flow with increasing Re. We note though that the destabilization is primarily due to ϕ_{ps1} , which represents the coupling of the stress gradient perturbation with the base state velocity since it increases rapidly near critical conditions. Stress gradients are indeed maximized near the cusp region, as shown in Fig. 8(c). ϕ_{pv2} , which represents the coupling of the velocity gradient perturbation with the base state stresses, appears to increase considerably, albeit at supercritical conditions. On the other hand, the magnitude of the term ϕ_{pv1} decreases rapidly close to criticality, indicating that the polymeric stress gradients of the base state tend to stabilize the fluid flow. Since ϕ_{ps1} is the most destabilizing term, we may deduce that in viscoelastic liquids an additional mechanism of instability exists which is related with the convection of the perturbation of the polymeric stress field by the base state fluid flow. Nevertheless, inertia remains the leading mechanism for the onset of instability.

3. Stability maps for disturbances with arbitrary wavelength: Effect of Wi

So far we have discussed the stability of an Oldroyd-B liquid for steady flows allowing only 2D long-wave disturbances, i.e., for $Q \ll 1$. In order to investigate the effect of disturbances with any wavelength, we produce the stability maps shown in Fig. 9 considering values of the Bloch wave number Q in the range $[0, 0.5]$. Figure 2(b) shows the stability map for the case of *Elbesil 65*, which is a Newtonian liquid; its properties are given in Table I. For disturbances with infinite wavelength ($f \rightarrow 0$) the Re_c is calculated to be 8.51, whereas the flow becomes first unstable for a finite value of the disturbance frequency, i.e., for $f = 0.052$ (which corresponds to $Q = 0.405$) and $\text{Re}_c = 5.09$. Note that this behavior in the case of structured surfaces is markedly different from the flow over an inclined flat surface in which the most unstable eigenmode corresponds to long-wave disturbances, i.e., for $f \rightarrow 0$. This effect has been observed experimentally [15,18] and has been attributed to the resonance of the steady free surface with the bottom wall [43]. We have already seen in Fig. 6(a) that for moderate values of Re ($15.79 \leq \text{Re} \leq 22.34$) the flow becomes stabilized. Note that the isle of stability also exists for finite frequency values, as can be clearly seen in Fig. 2(b).

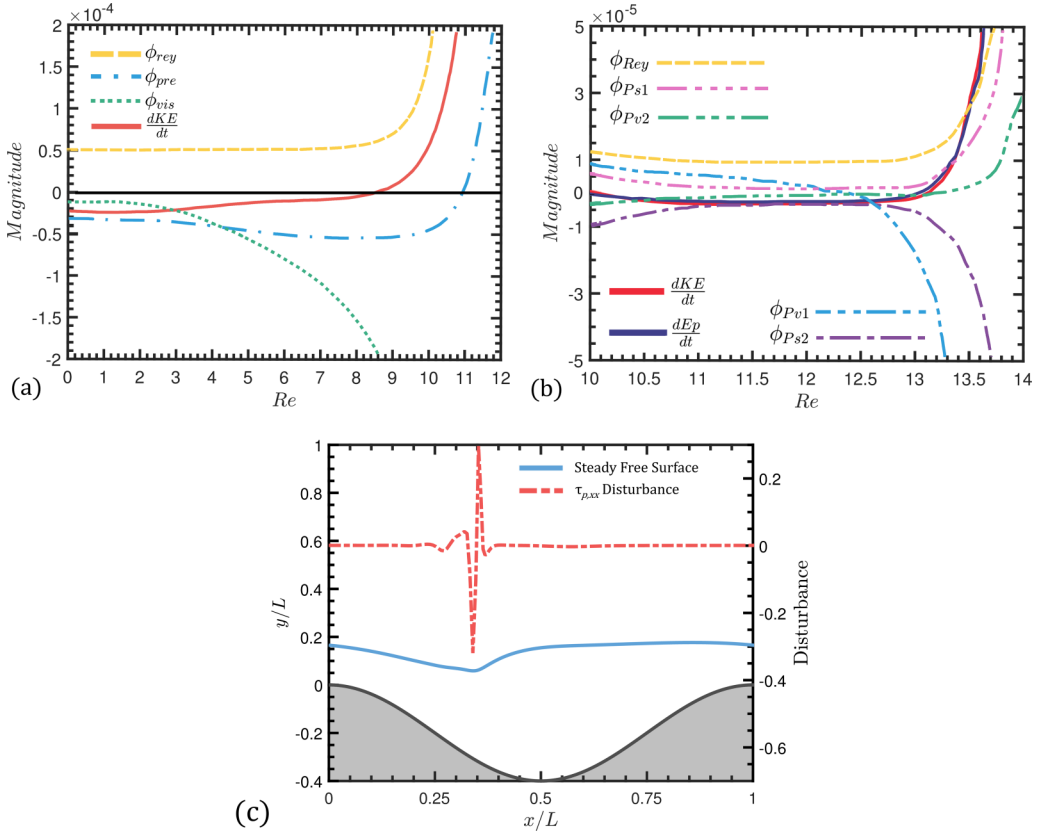


FIG. 8. Energy analysis diagrams for the leading mode for (a) Newtonian and (b) Oldroyd-B liquid, for $\varepsilon = 0$ and $Wi = 1$, under long-wave disturbances $Q = 10^{-2}$. (c) Steady free surface (continuous blue line) and its corresponding $\tau_{p,xx}$ disturbance for $Q = 10^{-2}$ (red dashed dotted line) calculated at $Re = 9.1$. The remaining parameters are $Wi = 1$, $\varepsilon = 0$.

With increasing fluid elasticity, the flow progressively deviates from the Newtonian case, as can be seen in Figs. 9(a)–9(d) for $Wi = 0.5, 0.75, 1$, and 1.5 , respectively. For $Wi = 0.5$ [Fig. 9(a)] the stability map differs in two ways from that of a Newtonian liquid. First, as also seen in Fig. 6(a), we have the appearance of two isles of stability instead of one for a Newtonian liquid; and secondly for low values of elasticity the flow appears to become more stable since the first critical Re increases to 6.89 (for $f = 0.046$ which corresponds to $Q = 0.324$). In this case, elasticity acts in a different way than in Nusselt flow [24] due to the spatial variation of the steady normal polymeric stresses (see Fig. 5 in Part I) which provides a significant stabilizing effect on the flow at finite values of Q . Nevertheless, for higher values of Re , due to the effect of elasticity, stable isles arise with considerably smaller size than in the Newtonian counterpart. Further increase of Wi [Fig. 9(b)] indicates that the bulk fluid elasticity has an overall stabilizing effect on the fluid flow, and the most unstable state is now encountered for long-wave disturbances ($f \rightarrow 0$). Therefore, we deduce that the elasticity is responsible for dampening high frequency interfacial perturbations. Interestingly, the stable isle in the range of $Re \sim 17.5 - 22$ expands its area, and for the even higher value of Wi [Fig. 9(c)] it crosses the main neutral curve connecting the two stable regimes. An unstable isle thus is created which contains a smaller stable isle for Re in the range between 10.31 and 13.23. Interestingly, even though the flow initially becomes unstable at $Re_c = 7.3$, there is a stable region for Re in $17.4 < Re < 21.8$, denoting that the fluid elasticity induces a small window where all

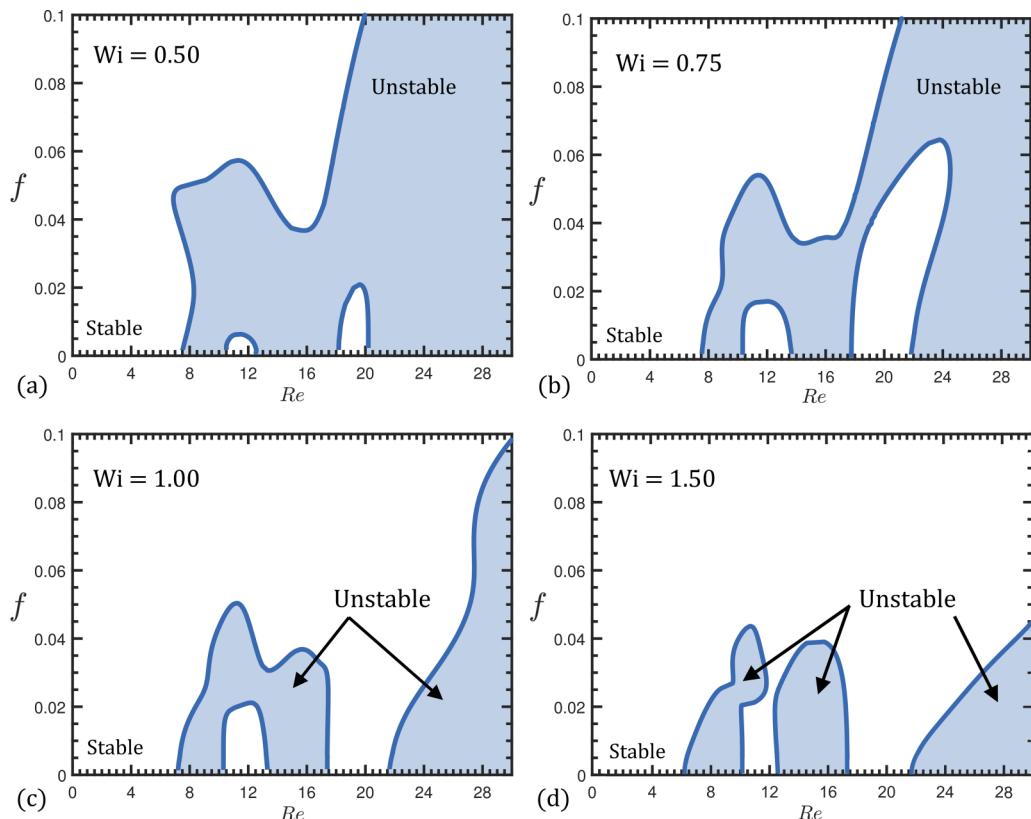


FIG. 9. Effect of the Wi number in the stability diagrams using the Oldroyd-B model. (a) $Wi = 0.5$, (b) $Wi = 0.75$, (c) $Wi = 1.0$, (d) $Wi = 1.5$.

linear perturbations are dampened at supercritical conditions. With an additional increase of Wi , the unstable isle shrinks further and at $Wi = 1.5$ it is split into two smaller unstable isles; see Fig. 9(d). Clearly, the unstable isles correspond to the first and second resonance points described in Fig. 6(a) while the neutral curve that arises for $Re > 22$ [see Fig. 9(d)] indicates the transition to instability due to the dominance of inertia in the fluid flow. This value is 4 times larger than the critical Re for a Newtonian liquid, $Re_c = 5.09$, which is a clear demonstration of the stabilizing effect of fluid elasticity.

B. Linear stability analysis for the ePTT fluid

1. Stability maps for disturbances with arbitrary wavelength: Effect of Wi

We now turn our attention to the case of an ePTT fluid, which may provide a better description for polymeric solutions because, besides the effect of elasticity, they also typically exhibit considerable shear thinning. In Fig. 10 we present stability maps for $Wi = 0.5$ and 1. We use a rather small value for the exponent $\varepsilon = 0.05$ and keep the remaining parameters as in Fig. 9. As shown in Fig. 10(a), for weak fluid elasticity the flow becomes slightly stabilized since the most critical Re , is found to be $Re_c = 5.56$, higher than the corresponding value for the Newtonian liquid, $Re_c = 5.09$; see Fig. 2(b). Moreover, the most unstable mode has a lower frequency, $f = 0.050$ (which corresponds to $Q = 0.384$), than that for the Newtonian liquid ($f = 0.052$ and $Q = 0.405$). It should be noted that for an ePTT fluid and such low values of Wi the effect of shear thinning is not dominant, since the product of ε and Wi is very small and appears in the ePTT exponent, Eq. (4); see also [44]. Hence

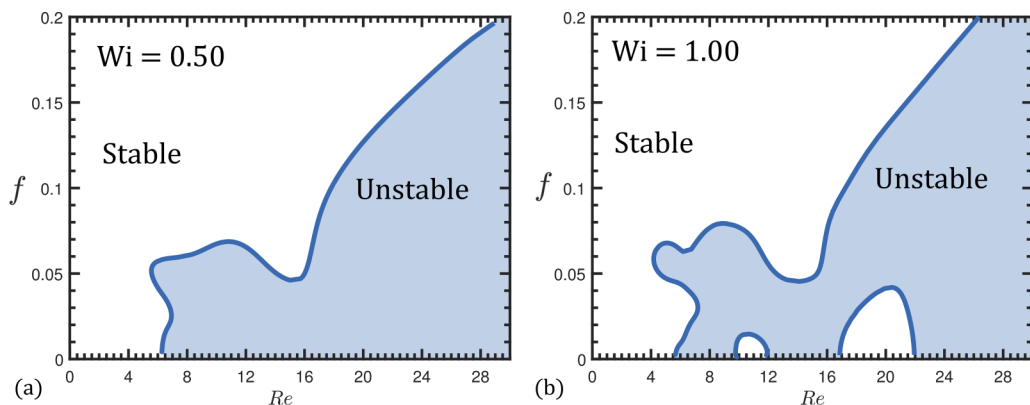


FIG. 10. Effect of the Wi number in the stability diagrams using the ePTT model for $\varepsilon = 0.05$. (a) $Wi = 0.5$, (b) $Wi = 1$.

the fluid exhibits behavior similar to the Oldroyd-B fluid [although with slightly lower value for Re_c compared to 6.89 for the Oldroyd-B fluid; see Fig. 9(a)], and therefore the stabilization of the flow, in this case, can be attributed to the elasticity alone. Even so, the presence of small shear thinning decreases the size of the stable isle, and for $Wi = 0.5$ it has completely disappeared; see Fig. 10(a). Increasing the value of Wi [see Fig. 10(b)], a different picture emerges, and the flow now becomes clearly destabilized, since the effect of shear thinning becomes stronger. We find that for $Wi = 1$ the most critical value of Re is $Re_c = 4.18$ while the most unstable mode has frequency $f = 0.059$ (corresponds to $Q = 0.45$) which is larger than the corresponding Newtonian case. It should be noted that the destabilizing effect of shear thinning has also been reported both experimentally and theoretically for film flows over a flat substrate of liquids following generalized Newtonian laws [21,22].

Figure 11(a) presents the stability map for the highest value of Wi that we have examined, i.e., for $Wi = 2$. Interestingly, in this figure, besides the further destabilization of the flow due to the increased effect of shear thinning, we also observe a discontinuity in the neutral curve which arises for $14.73 < Re < 14.89$. In this discontinuity the dimensionless frequency of the most unstable mode changes abruptly from 0.067 to 0.14. As already described in Part I, at this range of Re a hysteresis loop arises [see Fig. 11(b)], denoting the existence of multiple steady states in a narrow

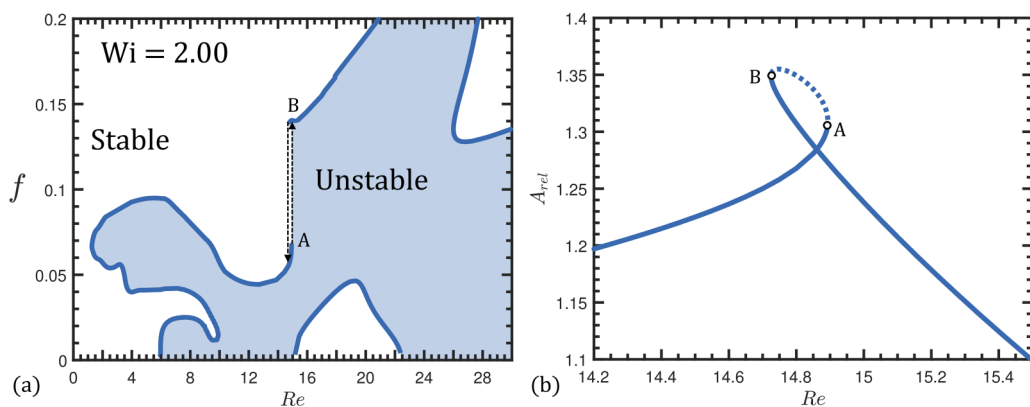


FIG. 11. (a) Stability diagram and (b) relative amplitude of the steady free surface, A_{rel} , close to the hysteresis loop, for $Wi = 2$ and $\varepsilon = 0.05$.

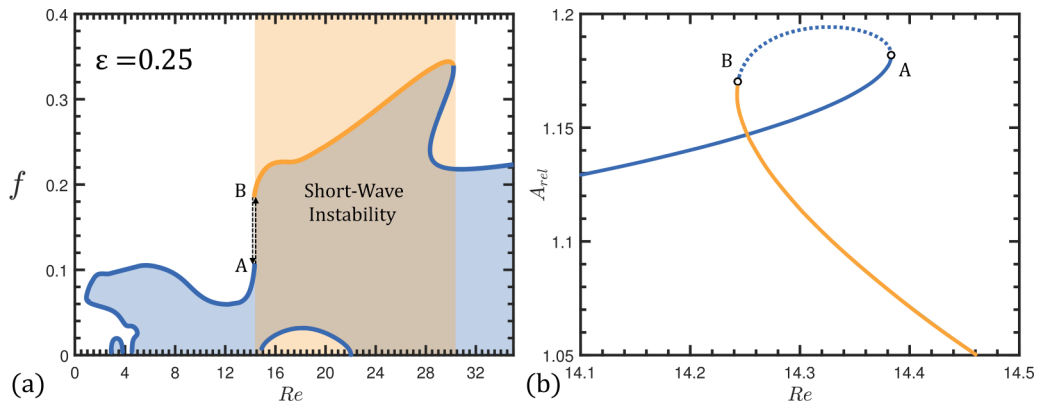


FIG. 12. (a) Stability diagram for $Wi = 1$, $\varepsilon = 0.25$ and (b) close-up of the relative amplitude of the free surface at steady solution, A_{rel} , corresponding to the jump in frequency.

range of Re . The points A and B in Fig. 11(a) depict the frequencies at the first and second turning point of the hysteresis loop of Fig. 11(b). We could not find a critical value for Re at the upper branch connecting these points in the hysteresis loop [see the dashed line in Fig. 11(b)], indicating that this branch is unstable for all values of Q . Indeed, examination of the eigenspectrum for this upper branch AB reveals that the eigenvalue, which otherwise remained at $0 + 0i$ (it is the point “M0” in Fig. 13 to be discussed subsequently) assumes a positive real part. Therefore, points A and B correspond to the usual limit points of bifurcation theory, where one real eigenvalue becomes positive at A and zero again at B. All other unstable eigenvalues discussed in this study are complex.

2. Effect of the parameter ε

In Fig. 12 we present the stability diagram of the flow for $\varepsilon = 0.25$ alongside the hysteresis loop that arises in the steady state solution. As we have already discussed regarding Fig. 10(b), for $\varepsilon = 0.05$ the flow becomes unstable for $Re_c = 4.18$ and the most unstable mode has frequency $f = 0.059$. For $\varepsilon = 0.25$ [see Fig. 12(a)], the flow becomes destabilized at much smaller $Re_c = 0.92$ with $f = 0.067$ (which corresponds to $Q = 0.73$). We also observe that with increasing ε the wavelength of the most unstable disturbance decreases (corresponding to the frequency increase). Generally, we note that for $\varepsilon = 0.25$ the range of critical frequencies has values almost twice as large as for $\varepsilon = 0.05$ [see Fig. 10(b)], which indicates that shear thinning promotes the occurrence of instability at shorter wavelengths. Furthermore, the discontinuity in the neutral curve that appears for $\varepsilon = 0.25$ is due to the presence of a hysteresis loop in the steady state flow that here arises for $14.28 < Re < 14.38$ [see Fig. 12(b)], similarly to the case in Fig. 11.

Interestingly, beyond point B in Fig. 12(a), the frequency of the disturbance increases further, while its wavelength becomes short enough to be less than the wavelength of the topography, which signifies the onset of the so-called “short-wave” instability. Essentially, the terms “long-wave” and “short-wave” refer to disturbances with wavelengths longer and shorter with respect to substrate undulations. Note that during this transition there is a critical point where the wavelength of the disturbance is identical to the wavelength of the substrate, so that it corresponds to $Q = 0$. In Fig. 13 we present the spectrum of the fluid flow just before the first turning point at $Re = 14.38$ and just after the second one at $Re = 14.28$ [Fig. 12(b)], while we mark with white circles the eigenmodes that arise for $Q = 0$. These modes are the harmonics of the steady free surface inside the unit cell; for instance, the modes “M1” and “M2” in Fig. 13 represent the first and second harmonics of the system, with wavelengths L and $L/2$, respectively, whereas the mode “M0” is pinned at $0 + 0i$ and it is described as the zeroth harmonic of the system. The rest of the spectrum (blue line) is generated for $Q \neq 0$. The eigenvalues that lie between the points M0 and M1 are responsible for

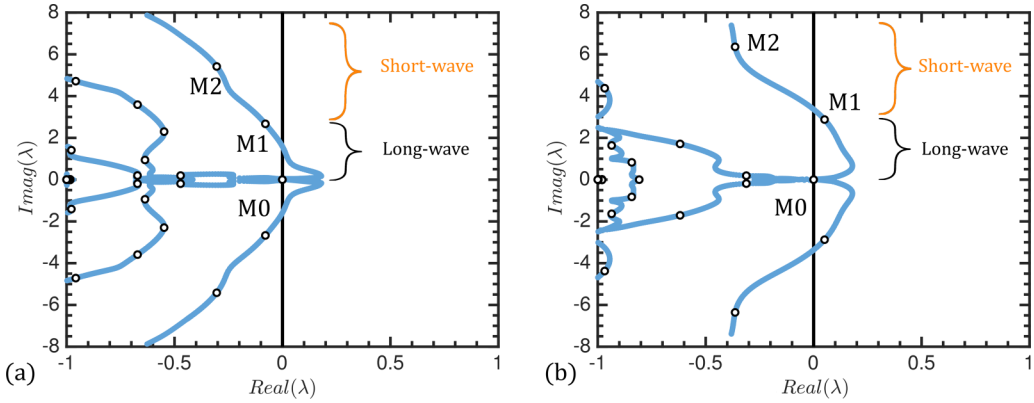


FIG. 13. Eigenspectrum calculated at (a) $Re = 14.37$ and (b) $Re = 14.28$ for $Wi = 1$ and $\varepsilon = 0.25$. The white circles indicate the eigenvalues for $Q = 0$, while the blue lines indicate the continuous spectrum for $Q \neq 0$.

the long-wave instabilities of the flow since their wavelength is always larger than the topography wavelength. On the other hand, the eigenvalues that have an imaginary part larger than M1 are short wave. In Fig. 13(a) we observe that the growth rate and the imaginary part of the most dangerous eigenvalue are $\lambda_R = 0.18$ and $\lambda_I = 0.16$ for $Q = 0.13$ (wavelength $7.7L$), respectively. According to the spectrum, the flow is stable under short-wave disturbances since the eigenvalues at M0, M1, M2 have negative growth rate [see Fig. 13(a)], but is unstable to long-wave disturbances.

After the hysteresis loop [i.e., beyond point B in Fig. 12(a)] the growth rate and the imaginary part of the most unstable eigenvalue are $\lambda_R = 0.18$ and $\lambda_I = 0.66$ for $Q = 0.21$, respectively; see Fig. 13(b). Interestingly, the first harmonic of the system is unstable as well, while its growth rate is $\lambda_R = 0.06$ and the corresponding imaginary part is $\lambda_I = 2.88$, which demonstrates that the frequency of this unstable mode is 4 times larger than the linearly critical eigenvalue. Since the two modes coexist and their growth rates are comparable to each other, we might expect that in this regime short-wave instability will be superposed on the low frequency (long-wave) disturbances and, given enough time, short-wave instabilities would also be observed in experiments. In Fig. 12(a) the light orange areas for $14.3 \leq Re \leq 30.22$ indicate the region where the first harmonic of the system is unstable, implying the short-wave instability. The continuous orange line in this figure depicts the frequency of the most dangerous mode for $Q = 0$ and provides an estimation for the frequency that could be observed in an experiment, because here the disturbance and topography wavelengths coincide. Cao *et al.* [17] have identified what they call “short-wave instability,” although the wavelength they observe is twice as long as that of the topography but still much shorter than the usual long wavelengths of thin film theory. Moreover, they state that this type of instability introduces an intrinsic frequency which is insensitive to external excitations. It is intriguing that the shorter waves with the smaller predicted growth rates are observed to dominate the longer ones. This may be caused by a difference in their phase velocities, but this is beyond the scope of this study. Schörner *et al.* [18] have observed that when short-wave instabilities arise, the stable isles are not observed. This is understandable, since there is at least one unstable eigenvalue and therefore the stable isle that arises for $14.88 \leq Re \leq 22.02$ will not be observed experimentally, simply because it exists only for specific (small) values of Q .

In Fig. 14 we present the steady free surface along with the disturbance profile of the most unstable mode, $Q = 0.2$, the first harmonic one, $Q = 0$, and their superposition with the base state profile. Both disturbances are unstable with wavelengths $5L$ and L , respectively. As we have already discussed, experiments indicate that eventually the first harmonic will dominate over the long-wave disturbance.

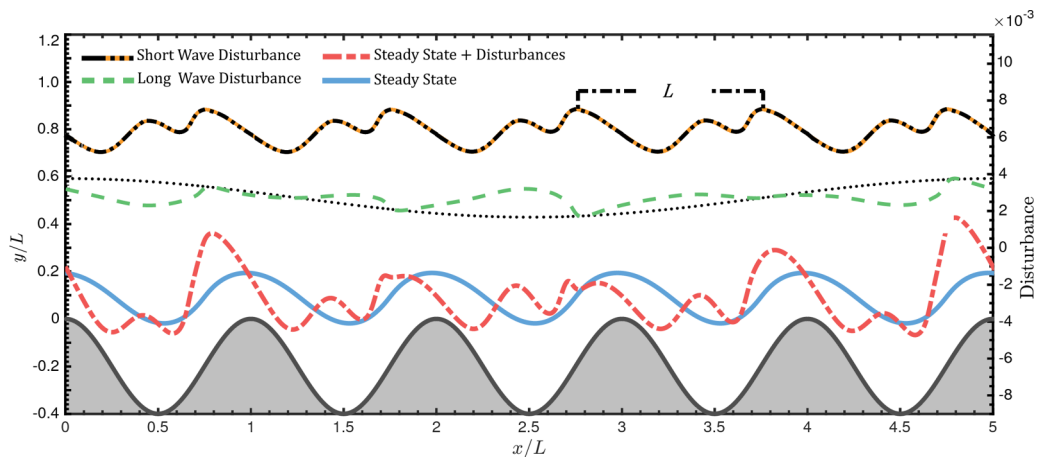


FIG. 14. Steady free surface and its disturbances for $Q = 0$ (black-orange dashed line) and $Q = 0.2$ (dashed green line), for $Re = 14.28$, $Wi = 1$, $\varepsilon = 0.25$. The red dash-dotted line indicates the superposition of the steady free surface (continuous blue line) and the corresponding disturbances, where the magnitude of the latter has been magnified 200 times. The black dotted line indicates the long-wave disturbances.

It is noteworthy that the regime of the short-wave instability is not sustained at higher values of Re and remains constrained in a region for $14.3 \leq Re \leq 30.22$ only. For higher values of Re , we find that short-wave instabilities are not possible and the flow becomes unstable only to long-wave disturbances, again. For $Re = 30.22$ the eigenmode M1 becomes stable and the frequency abruptly drops from $f = 0.34$ to 0.22 ; see Fig. 12(a). As will be explained below, this is mainly due to inertia, which eventually overwhelms shear thinning, which favors the emergence of high frequency modes. In Fig. 15 we depict the spatial variation of the polymeric shear stress, $\tau_{p,yx}$ and the normal polymeric stress field, $\tau_{p,xx}$, for the steady base state. We observe that for this limiting value of Re a large recirculation arises inside the wall corrugations (the continuous black lines in Fig. 15 depict the streamlines). As described by Nguyen and Bontozoglou [45] and Pollak and Aksel [15] such vortices arise at sufficiently high values of Re , depending on the amplitude of the wall corrugations, due to the effect of inertia. This eddy splits the fluid flow into two regions: the main stream region where a strong velocity field exists and a recirculation region where the flow is slower. The effect of shear thinning is mostly important in the mainstream region and is maximized near the crests of the wall corrugations [see Fig. 15(a)] as the recirculation region expands with increasing Re . As a result, only a small part of the total fluid flow is affected by the shear thinning of the fluid. On the other hand, due to the flow detachment at the upstream wall, the normal stresses of the polymeric solution acquire high values [see Fig. 15(b)] as the polymeric chains become extended to conform to the fluid flow. Therefore, for high values of Re elasticity dominates over shear thinning and the frequency of the most unstable disturbance decreases considerably.

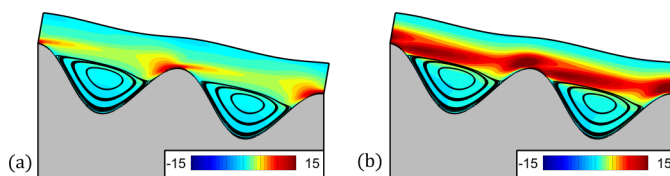


FIG. 15. Spatial variation of the steady (a) shear stress, $\tau_{p,yx}$, and (b) normal stress component, $\tau_{p,xx}$, of the polymeric stress tensor for $Re = 30.22$, $Wi = 1$, $\varepsilon = 0.25$.

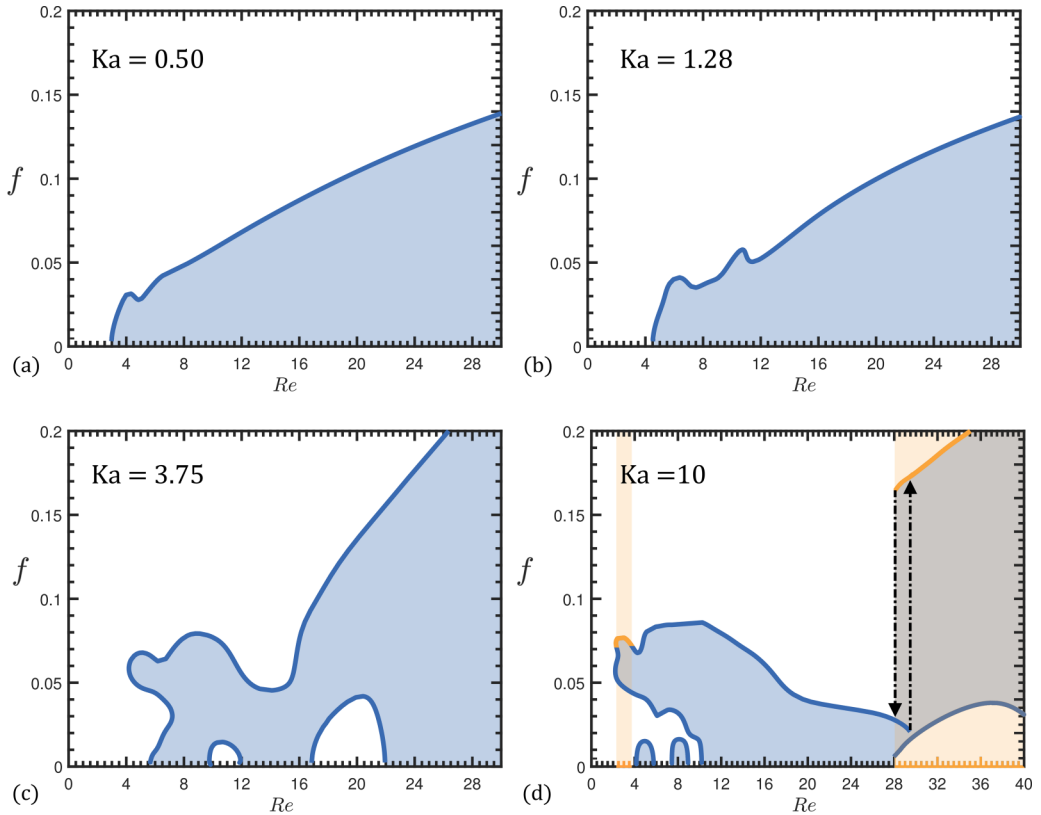


FIG. 16. Effect of Ka in the stability diagrams using the ePTT model for $Wi = 1$, $\varepsilon = 0.05$. (a) $Ka = 0.5$, (b) $Ka = 1.28$, (c) $Ka = 3.75$, (d) $Ka = 10$.

3. Effect of zero shear viscosity

In Fig. 16 we present stability maps for different values of Ka . By changing the value of the Kapitza number while keeping the ratio $L = L^*/l_c^*$ constant, we consider cases with varying l_v^* [see Eq. (16) in Part I]. Therefore, for liquids with the same density, by varying the value of Ka we consider liquids with different zero-shear viscosities; the smaller the value of Ka , the more viscous the liquid is. In Fig. 16(a) we present the case of a highly viscous liquid with $Ka = 0.5$. We observe that the neutral curve acquires an almost semiparabolic profile as for Newtonian very viscous liquids, while the flow becomes unstable for $Re_c = 2.98$ under long-wave disturbances. We should note that under constant flow rate the film is thicker when its viscosity increases; this can also be inferred from Eq. (16) in Part I. Due to the increased distance between the interface and the substrate, the steady free surface remains relatively smooth and does not interact significantly with the wavy wall, which explains why we do not see any signs of resonance in this map. For $Ka = 1.28$ [see Fig. 16(b)], the substrate mildly interacts with the free surface of the film and thus small fluctuations on the neutral curve arise, even if the flow remains unstable under long-wave disturbances.

The pattern changes dramatically for liquids with lower viscosity, e.g., Figs. 16(c) and 16(d), where we depict stability maps for $Ka = 3.75$ and 10 and the flow becomes unstable for $Re_c = 4.18$ and $f = 0.056$ ($Q = 0.45$) and $Re_c = 2.21$, $f = 0.057$ ($Q = 0.74$), respectively. In these cases, the films are thinner and thus allowed to resonate with the topography of the substrate. As noted in the discussion of Fig. 7 in Part I, the interaction of the steady free surface with the substrate gives rise to a cusp which tends to destabilize the flow. In Fig. 16(d), we also notice that even at the

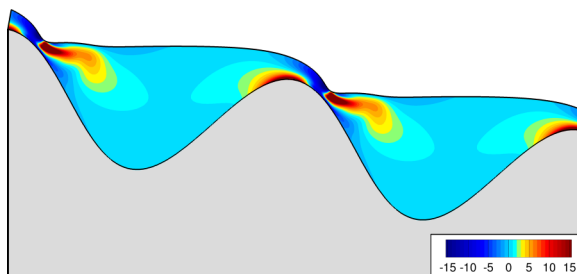


FIG. 17. Steady shear stress component of the polymeric stress tensor, $\tau_{p,yx}$, for $Re = 3$, $Wi = 1$, $\epsilon = 0.05$, $Ka = 10$.

most critical value of Re ($Re_c = 2.21$) a long-wave instability arises. However, for slightly higher values of Re there is a transition to short-wave instability in the range $2.27 \leq Re \leq 3.1$. This could be attributed to the intense shear stress field that arises close to the descending part of the wall, producing high-velocity gradients at the liquid-air interface (see Fig. 17 where we present the steady spatial variation of $\tau_{p,yx}$). Due to its decreased viscosity and shear thinning, the mean flow velocity increases and thus the film height decreases close to the descending part of the wall, producing an intense depression at the interface. This intensifies locally the shear stresses, leading to stronger shear thinning. With increasing Re the depression of the free surface moves downstream, reducing the strong stress field at the crest of the wall, and the instability of the fluid flow becomes long wave again. Finally, for $Ka = 10$, our steady calculations show that the resonance point of the steady free surface with the substrate arises at $Re = 29.47$. For this value of Re , a hysteresis loop arises (similar to the one described in Fig. 7 in Part I), which is the reason for the frequency discontinuity in the stability map. Beyond this critical value of Re , a short-wave instability arises which dominates the stability of the flow, as described in Fig. 12.

4. Effect of the Newtonian solvent

In Fig. 18 we present the effect of the Newtonian solvent viscosity in the viscoelastic fluid by increasing the parameter $\beta = 0.4$ of the ePTT model. This increase causes a weak stabilization of the flow, since for $\beta = 0.1$ the most critical Re was calculated to be $Re_c = 4.18$ for $f = 0.056$

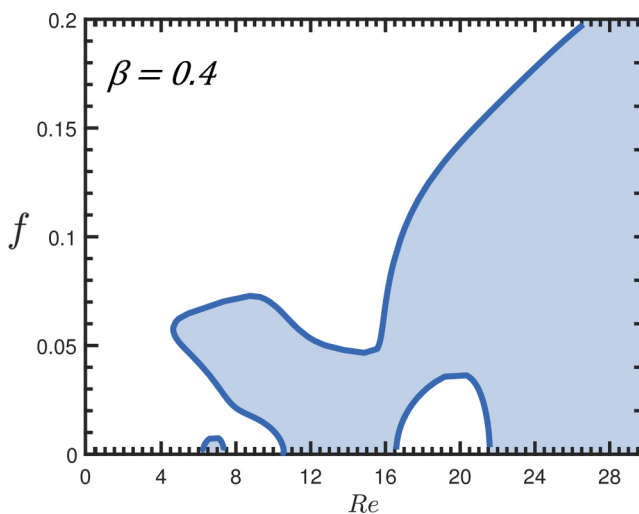


FIG. 18. Effect of β in the stability diagrams using the ePTT model for $Wi = 1$, $\epsilon = 0.05$, $\beta = 0.4$.

TABLE III. Properties of the polymeric solutions.

Viscoelastic liquid	Density (kg/m ³)	Zero-shear		Relaxation time λ_e^* (s)	Kapitza number Ka	Elasticity number El
		viscosity (mPa s)	$\beta = \frac{\mu_s^*}{\mu^*}$			
VS1	958	62.2	0.1	0.008	3.75	1.0
VS2	958	62.2	0.1	0.043	3.75	5.0
VS3	958	62.2	0.1	0.087	3.75	10

[$Q = 0.45$, Fig. 10(b)], while for $\beta = 0.4$ we get $Re_c = 4.65$ for $f = 0.057$ ($Q = 0.4$, Fig. 18). We notice that for disturbances with high frequency the neutral curves remain almost unaffected, while for disturbances with low frequency the flow becomes significantly stabilized with increasing β . It is interesting to note that, as $f \rightarrow 0$, the critical Re was computed at 5.63 and 10.55, for $\beta = 0.1$ and 0.4, respectively. Naturally, increasing β further will lead to a neutral curve with a form similar to that for a Newtonian fluid. However, above $\beta = 0.4$, the liquid is considered as a dilute polymer solution in which different phenomena may arise such as polymer migration that cannot be described by the ePTT model [46].

5. Effect of relaxation time

In order to examine the effect of the relaxation time of the viscoelastic liquid on the stability of the flow, we define the elasticity number by scaling the relaxation time of the polymeric solution λ_e^* with the viscous timescale $t_v^* = (\frac{\mu^*}{\rho^* g^{*2}})^{1/3}$:

$$El = \frac{\lambda_e^*}{t_v^*} \equiv \lambda_e^* \frac{\rho^{*\frac{1}{3}} g^{*\frac{2}{3}}}{\mu^{*\frac{1}{3}}} \quad (26)$$

The definition of this number could be advantageous for an experimentalist because it depends only on physical properties of the liquid such as the relaxation time, zero-shear viscosity, and liquid density. The relation between this and Weissenberg number is given by the expression:

$$Wi = El Re^{1/3} St^{-2/3} \quad (27)$$

Clearly, by changing this parameter while keeping Ka constant, we can describe the effect of the relaxation time of viscoelastic fluid independently of the flow rate. Typical values for El are given in Table III, corresponding to data of liquids that have been used in experiments of coating flows, e.g., solutions of polyethylene oxide (PEO) or Poly-methyl-methacrylate (PMMA) [47–51].

Figures 19(a) and 19(b) depict the stability maps for $El = 1, 5$, respectively. Note that, for a constant elasticity number, while Re increases, the Wi number varies according to Eq. (27). For example, when $El = 5$, the Weissenberg number varies between 0 and 2.5 in the range of Re depicted in Fig. 19(b). The parameter ε of the ePTT model has been set to $\varepsilon = 0.20$, and therefore here we consider liquids with intense shear thinning. For $El = 1$ the stability map remains almost unaffected in comparison to that for Newtonian liquids, while the most unstable mode has frequency $f = 0.055$ (which corresponds to $Q = 0.38$) for $Re_c = 4.8$. When $El = 5$ the short-wave mode arises for $13.5 < Re < 28$, with a hysteresis loop in the low end of Re and an abrupt decrease in the frequency above the high end. When $El = 10$, short-wave instabilities arise also for $1 < Re < 4$. Generally, increasing El instability arises at smaller Re and for finite frequencies.

6. Flow subjected to 3D disturbances

Here, we investigate the stability of the flow when subjected to disturbances in the spanwise direction, given that Squire's theorem does not hold even for shear-thinning fluids (without elasticity) flowing over a flat substrate [50]. To this end, we examine the effect of Wi under the

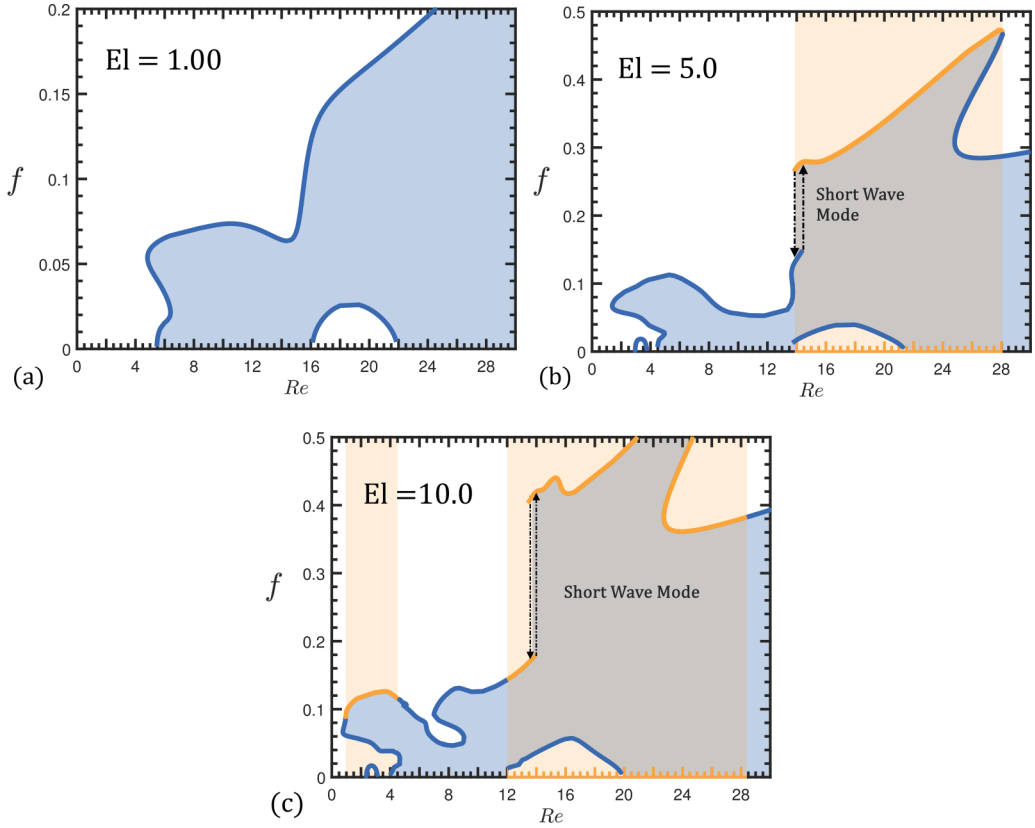


FIG. 19. Effect of El in the stability diagrams using the ePTT model for $\varepsilon = 0.20$. (a) $El = 1$, (b) $El = 5$, and (c) $El = 10$.

constant value of $Re = 10$, while assuming $Q = 0$; i.e., we examine disturbances with wavelength in the streamwise direction equal to the wavelength of the substrate. In Fig. 20(a) we present dispersion curves for different values of Wi . For $Wi = 1$, the growth rate is negative for all values of

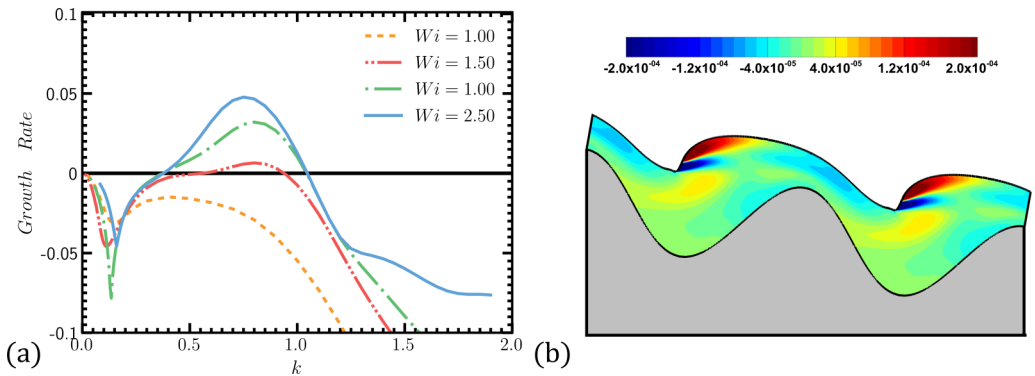


FIG. 20. (a) Dispersion curves for disturbances in the spanwise direction for $Q = 0$ for $Wi = 1.0, 1.5, 2.0$ shown with dashed lines, while $Wi = 2.5$ is presented with the continuous line. (b) Disturbances of the spanwise velocity component, $u_{z,d}(x, y)$, for $k = 0.75$, $Wi = 2.5$, $\varepsilon = 0.15$, and $Re = 10$.

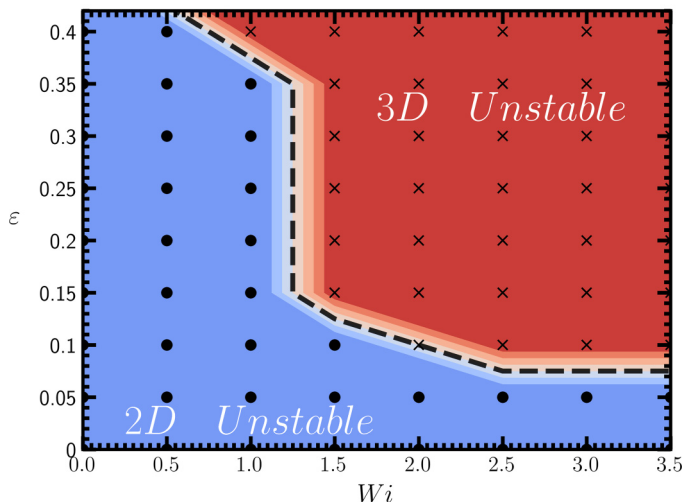


FIG. 21. Stability map in the (Wi, ε) plane for the onset of 3D instabilities for $Re = 10$, $Ka = 3.75$, and $\beta = 0.10$.

k , indicating that the fluid flow is stable with respect to 3D disturbances. Increasing the value of Wi , the growth rate of the disturbance is shifted closer to the neutral stability line, showing a tendency of the flow to become unstable. Interestingly, at $Wi \approx 1.5$, the dispersion curve crosses the neutral stability line, indicating that the flow becomes unstable to 3D disturbances with wave number larger than $k = 0.56$, while the maximum growth rate arises at $k = 0.81$; the cutoff wavenumber beyond which surface tension stabilizes the flow is equal to $k = 0.93$. Increasing further the value of Wi , the growth rate increases as well, while the wave number of the most unstable modes shifts to smaller values, i.e., $k = 0.79, 0.75$ for $Wi = 2.0$ and 2.5 , respectively.

Therefore, it becomes evident that for this particular case, when the flow is subjected to L -periodic disturbances in the streamwise direction and above a specific value of Wi , the flow becomes unstable, forming 3D structures. As shown in Fig. 20(b), the spatial variation of the z component of the velocity disturbance, $u_{z,d}$, appears to be localized around the area where the static hump arises. It is also worth noting that the 3D instability of fluid flow appears up to the resonance point ($Re \approx 14$) because after that point the deformation of the free surface relaxes, leading to the disappearance of the cusp in the steady free surface. The critical conditions for the onset of the 3D instabilities as liquid elasticity and shear thinning vary are shown in Fig. 21. In this figure, the bullet and cross points in the (Wi, ε) plane indicate whether the flow is found to be most unstable to 2D or 3D instabilities, respectively; the dashed line indicates critical conditions for the transition between the two states. We observe that the 2D disturbances are most dangerous in the case of weakly viscoelastic liquids (low values of Wi) or for liquids that do not exhibit significant effect of shear thinning (low values of ε and Oldroyd-B fluids). In both these limits, the steady free surface does not exhibit a cusp and the flow was found to be most unstable under 2D long-wave disturbances. 3D instabilities arise in the top-right corner of the (Wi, ε) plane for either highly elastic liquids or liquids with intense shear thinning. Obviously, the velocity gradients that arise near the cusp tend to destabilize the flow also in the spanwise direction. Nevertheless, it should be mentioned that the study in Fig. 21 concerns disturbances that have the same periodicity with the substrate (i.e., for $Q = 0$). However, our parametric study above has indicated that, as far as infinitesimal disturbances are concerned, i.e., in the limit of linear stability, long-wave 2D instabilities are always observed first in the system, and therefore the 3D disturbances shown here most probably provide a secondary mechanism for the destabilization of the flow. In order to be more conclusive on this matter, further study would be required, which, however, is out of the scope of the present work.

VI. SUMMARY AND CONCLUSIONS

We carried out a theoretical analysis of the linear stability of a viscoelastic liquid film flowing down an inclined sinusoidal surface and performed a detailed parametric study for a wide range of material properties. Our results are in excellent agreement with the previous theoretical [18] and experimental [19] results in the case of Newtonian liquids flowing over flat and undulating substrates and viscoelastic liquids over flat substrates [26]. For viscoelastic liquids, linear stability predicts a robust stabilization of the fluid flow due to the presence of fluid elasticity. In particular, the spatial variation of steady normal polymeric stresses of the flow creates a force that opposes inertia and tends to damp the disturbances for all frequencies; the damping increases with increasing Wi . Energy analysis validated the latter mechanism, while it revealed an additional mechanism of instability which is related to the convection of the perturbation of the polymeric stress field by the base state fluid flow. Moreover, shear thinning destabilizes the flow, by increasing the effective inertia particularly around the maxima of the topography. Moreover, shear thinning increases the frequency of the instability, while at moderate values of Re there is a transition from long-wave disturbances to short-wave, i.e., disturbances with a shorter wavelength than the substrate wavelength. This type of instability introduces an intrinsic frequency which is insensitive to external excitations [17]. Finally, aside from 2D linear stability analysis, we determined the flow stability when subjected to disturbances in the spanwise direction. We found that at large values of Wi the pronounced cusp at the steady free surface becomes sharp, which triggers the instability to become 3D. The properties of this instability need further investigation, which is outside of the purpose of this study.

The current study provides a theoretical analysis of the effect of viscoelasticity and shear thinning on the stability of film flow over undulated topography. Experimental studies would be very useful for verification of the findings with different polymeric solutions. From a theoretical point of view, the effect of the inclination angle and shape of the substrate on the stability of the viscoelastic fluid flow could be studied further. Additionally, recent studies in Newtonian liquids report that the evolution of gravity-driven nonlinear traveling waves introduces new phenomena such as the abrupt collapse of high amplitude waves, which generates waves with smaller amplitude [51]. However, the effects of viscoelastic mechanisms in these phenomena have not been studied yet. Moreover, stability of thin films over hydrophobic surfaces (surfaces with microstructures forming gas inclusions) is another subject for future work. In these flow configurations the thin film partially wets the substrate and thus air is entrapped inside the topographical features [52,53]. The interaction between the primary free surface and the second free surface that lies inside the cavity of the substrate may provide a stabilization mechanism for the flow. The latter study is under way.

ACKNOWLEDGMENTS

The research work was supported by the Hellenic Foundation for Research and Innovation (HFRI) and the General Secretariat for Research and Technology (GSRT), under the HFRI Ph.D. Fellowship grant (Grant Agreement No. 1473) and the LIMMAT Foundation under the grant MuSiComPS. G.K. would like to acknowledge Hellenic Foundation for Research and Innovation (HFRI) and the General Secretariat for Research and Technology (GSRT), under Grant Agreement No. 792.

APPENDIX A: FORMULATION OF THE LINEAR STABILITY ANALYSIS PROBLEM

1. Finite element discretization

In order to account for 3D disturbances, we have employed Fourier modes in the transverse ζ direction; k denotes the wave number of the perturbation in the ζ direction. Therefore according to

our ansatz the disturbances are given by the following finite element interpolation:

$$\mathbf{u}'_d(\eta, \xi, \zeta) = \sum_i \hat{\mathbf{u}}^i \cdot [\phi^i(\eta, \xi) \mathbf{D}(k\zeta)], \quad (\text{A1})$$

$$P'_d(\eta, \xi, \zeta) = \sum_i \hat{P}^i \psi^i(\eta, \xi) \cos(k\zeta), \quad (\text{A2})$$

$$\mathbf{G}'_d(\eta, \xi, \zeta) = \sum_i \hat{\mathbf{G}}^i_d : [\psi^i(\eta, \xi) \mathbf{E}(k\zeta)], \quad (\text{A3})$$

$$\boldsymbol{\tau}'_{p,d}(\eta, \xi, \zeta) = \sum_i \hat{\boldsymbol{\tau}}^i_{p,d} : [\chi^i(\eta, \xi) \mathbf{E}(k\zeta)], \quad (\text{A4})$$

$$\mathbf{x}'_d(\eta, \xi, \zeta) = \sum_i \hat{\mathbf{x}}^i_d \phi^i(\eta, \xi) \cos(k\zeta). \quad (\text{A5})$$

The symbol “:” denotes the double inner product. In a fashion similar to the approach described by [31,54], we choose a control volume consisting of the two-dimensional flow domain extended over one wavelength in the z direction and employ weighting functions of the form $\phi^i \mathbf{D}(k\zeta)$ for the momentum equations, $\psi^i \cos(k\zeta)$ for the continuity equations, $\chi^i \mathbf{E}(k\zeta)$ for the constitutive equations, $\psi^i \mathbf{E}(k\zeta)$ for the continuous approximation of the gradient tensor, and $\phi^i \cos(k\zeta)$ for the mesh equations; k denotes the wave number of the perturbation in the ζ direction. The tensors $\mathbf{D}(k\zeta)$ and $\mathbf{E}(k\zeta)$ are given by

$$\mathbf{D}(k\zeta) = \begin{pmatrix} \cos k\zeta & 0 & 0 \\ 0 & \cos k\zeta & 0 \\ 0 & 0 & \sin k\zeta \end{pmatrix}, \quad (\text{A6})$$

$$\mathbf{E}(k\zeta) = \begin{pmatrix} \cos k\zeta & \cos k\zeta & \sin k\zeta \\ \cos k\zeta & \cos k\zeta & \sin k\zeta \\ \sin k\zeta & \sin k\zeta & \cos k\zeta \end{pmatrix}, \quad (\text{A7})$$

and their form is dictated by the incompressibility condition and the kinematic relation at the free surface [31,54–56].

2. Linearized equations

The linearized equations are obtained using the weak formulation of the time-dependent form of the governing equations; introducing eq. (13) and neglecting terms of order higher than the first in the perturbation parameter δ , the following set of linearized equations is obtained from the corresponding momentum and mass balances, respectively:

$$\begin{aligned} & \int_V [(\text{Re } \mathbf{u}_b \cdot (\nabla \mathbf{u})_b - St \mathbf{g}) \cdot \mathbf{r}^i_j - P_b \mathbf{I} : (\nabla \mathbf{r}^i_j)_b + \boldsymbol{\tau}^T_{EVSS,b} : (\nabla \mathbf{r}^i_j)_b] J_{2D,d} dV \\ & + \int_V \left[\text{Re} \left(\frac{\partial \mathbf{u}_d}{\partial t} + \mathbf{u}_b \cdot (\nabla \mathbf{u})_d + \left(\mathbf{u}_d - \frac{\partial \mathbf{x}_d}{\partial t} \right) \cdot (\nabla \mathbf{u})_b \right) \right] \cdot \mathbf{r}^i_j J_{2D} dV \\ & + \int_V [-P_b \mathbf{I} : (\nabla \mathbf{r}^i_j)_d - P_d \mathbf{I} : (\nabla \mathbf{r}^i_j)_b + \boldsymbol{\tau}^T_{EVSS,d} : (\nabla \mathbf{r}^i_j)_b + \boldsymbol{\tau}^T_{EVSS,b} : (\nabla \mathbf{r}^i_j)_d] J_{2D} dV \quad (\text{A8}) \\ & - \int_{\partial V} \mathbf{n}_b \cdot (-P_b \mathbf{I} + \boldsymbol{\tau}^T_{EVSS,b}) \cdot \mathbf{r}^i_j J_{1D,d} dA \\ & - \int_{\partial V} [\mathbf{n}_d \cdot (-P_b \mathbf{I} + \boldsymbol{\tau}_{EVSS,b}) + \mathbf{n}_b \cdot (-P_d \mathbf{I} + \boldsymbol{\tau}_{EVSS,d})] \cdot \mathbf{r}^i_j J_{1D} dA = 0, \quad j = x, y, z, \end{aligned}$$

$$\int_V [(\nabla \cdot \mathbf{u})_d J_{2D} + (\nabla \cdot \mathbf{u})_b J_{2D,d}] \psi^i \cos k\zeta dV = 0, \quad (\text{A9})$$

where

$$\mathbf{r}_j^i = \mathbf{e}_j \cdot \phi^i \mathbf{D}(k\zeta). \quad (\text{A10})$$

The expression for the base state and perturbation of the total stress is readily obtained from

$$\boldsymbol{\tau}_{EVSS,i} = \boldsymbol{\tau}_{p,i} + 2(1 - \beta)\dot{\boldsymbol{\gamma}}_i - 2(\mathbf{G}_i + \mathbf{G}_i^T), \quad i = b, d. \quad (\text{A11})$$

Moreover, $J_{2D,d} = (y_{b,\xi} x_{d,\eta} - y_{b,\eta} x_{d,\xi}) + (y_{d,\xi} x_{b,\eta} - y_{d,\eta} x_{b,\xi})$ and $J_{1D,d} = \frac{(x_{b,\Gamma} x_{d,\Gamma} + y_{b,\Gamma} y_{d,\Gamma})}{\sqrt{x_{b,\Gamma}^2 + y_{b,\Gamma}^2}}$, while $dV = d\eta d\xi d\zeta$ and $dA = d\Gamma d\zeta$ are the differential volume and surface area in the computational domain, respectively; J_{2D} and J_{1D} are given in Part I (see Appendix). It should be noted that integration over one wavelength in the ζ direction ultimately gives a common factor of $\pi/2$ which can be safely ignored; this is due to the ζ dependence that arises in factors of $\cos^2 k\zeta$ and $\sin^2 k\zeta$ in the weak form of the equations.

The disturbance of the continuous approximation of the components of the velocity gradient tensor is determined by

$$\int_V (\mathbf{G}_d - (\nabla \mathbf{u})_d) : \mathbf{E}(k\zeta) \psi^i J_{2D} dV + \int_V (\mathbf{G}_b - (\nabla \mathbf{u})_b) : \mathbf{E}(k\zeta) \psi^i J_{2D,d} dV = 0 \quad (\text{A12})$$

The linearized PTT constitutive model becomes

$$\begin{aligned} & \int_V [Y(\boldsymbol{\tau}_{p,b})\boldsymbol{\tau}_{p,b} + Wi \overset{\nabla}{\boldsymbol{\tau}}_{p,b} - (1 - \beta)(\mathbf{G}_b + \mathbf{G}_b^T)] : \mathbf{E}(k\zeta) \chi_d^i J_{2D} dV \\ & + \int_V [Y(\boldsymbol{\tau}_{p,b})\boldsymbol{\tau}_{p,b} + Wi \overset{\nabla}{\boldsymbol{\tau}}_{p,b} - (1 - \beta)(\mathbf{G}_b + \mathbf{G}_b^T)] : \mathbf{E}(k\zeta) \chi_b^i J_{2D,d} dV \\ & + \int_V [Y(\boldsymbol{\tau}_{p,b})\boldsymbol{\tau}_{p,d} + Wi \overset{\nabla}{\boldsymbol{\tau}}_{p,d} - (1 - \beta)(\mathbf{G}_d + \mathbf{G}_d^T)] : \mathbf{E}(k\zeta) \chi_b^i J_{2D} dV \\ & + \int_V \left[\frac{\varepsilon}{1 - \beta} Wi \text{trace}(\boldsymbol{\tau}_{p,d})\boldsymbol{\tau}_{p,b} \right] : \mathbf{E}(k\zeta) \chi_b^i J_{2D} dV = 0. \end{aligned} \quad (\text{A13})$$

Here, the disturbance of the upper convective derivative is defined as

$$\begin{aligned} \overset{\nabla}{\boldsymbol{\tau}}_{p,d} = & \frac{\partial \boldsymbol{\tau}_{p,d}}{\partial t} + \left(\mathbf{u}_d - \frac{\partial \mathbf{x}_d}{\partial t} \right) \cdot (\nabla \boldsymbol{\tau}_p)_b + \mathbf{u}_b \cdot (\nabla \boldsymbol{\tau}_p)_d \\ & - [\boldsymbol{\tau}_{p,d} \cdot \mathbf{G}_b + (\boldsymbol{\tau}_{p,d} \cdot \mathbf{G}_b)^T] - [\boldsymbol{\tau}_{p,b} \cdot \mathbf{G}_d + (\boldsymbol{\tau}_{p,b} \cdot \mathbf{G}_d)^T]. \end{aligned} \quad (\text{A14})$$

In addition, χ_b^i and χ_d^i denote the base state weighting function χ^i and its perturbation, respectively. The former was defined in Part I (see Appendix), while the latter is given by the following expression:

$$\chi_d^i = \psi^i + \frac{h_{ch,b}}{|\mathbf{u}_b|} \left[\left(\mathbf{u}_d - \frac{\partial \mathbf{x}_d}{\partial t} \right) \cdot (\nabla \psi^i)_b + \mathbf{u}_b \cdot (\nabla \psi^i)_d \right] + \left(\frac{h_{ch,d}}{|\mathbf{u}_b|} - \frac{h_{ch,b} |\mathbf{u}_d - \frac{\partial \mathbf{x}_d}{\partial t}|}{|\mathbf{u}_b|^2} \right) \mathbf{u}_b \cdot (\nabla \psi^i)_b, \quad (\text{A15})$$

where $|\mathbf{u}_b|$ and $|\mathbf{u}_d - \frac{\partial \mathbf{x}_d}{\partial t}|$ denote the magnitude of the base state mean velocity and its perturbation, respectively. $h_{ch,b}$ denotes the characteristic length in each element at the base state domain and $h_{ch,d}$ denotes the disturbance in the perturbed domain.

Finally, the linearized weak formulation for the mesh generation equation is given by

$$\begin{aligned} & \int_V [(\nabla_{xy}(\phi^i \cos k\zeta))_b \cdot (\nabla_{xy}\xi)_d] [(1 - \varepsilon_1) + \varepsilon_1 S] J_{2D} dV \\ & + \int_V [(\nabla_{xy}(\phi^i \cos k\zeta))_d \cdot (\nabla_{xy}\xi)_b] [(1 - \varepsilon_1) + \varepsilon_1 S] J_{2D} dV \end{aligned}$$

$$\begin{aligned}
 & + \int_V [(\nabla_{xy}(\phi^i \cos k\zeta))_b \cdot (\nabla_{xy}\xi)_b] [(1 - \varepsilon_1) + \varepsilon_1 S] J_{2D,d} dV \\
 & + \int_V [(\nabla_{xy}(\phi^i \cos k\zeta))_b \cdot (\nabla_{xy}\xi)_b] \varepsilon_1 S_d J_{2D} dV = 0,
 \end{aligned} \tag{A16}$$

$$\begin{aligned}
 & \int_V [(\nabla_{xy}(\phi^i \cos k\zeta))_b \cdot (\nabla_{xy}\eta)_d] J_{2D} dV \\
 & + \int_V [(\nabla_{xy}(\phi^i \cos k\zeta))_d \cdot (\nabla_{xy}\eta)_b] J_{2D} dV \\
 & + \int_V [(\nabla_{xy}(\phi^i \cos k\zeta))_b \cdot (\nabla_{xy}\eta)_b] J_{2D,d} dV,
 \end{aligned} \tag{A17}$$

where $\nabla_{xy} = (\partial_x, \partial_y, 0)$ denotes the 2D gradient operator for Cartesian coordinates, while the definition for S_d is

$$S_d = (x_{b,\xi}x_{d,\xi} + y_{b,\xi}y_{d,\xi}) - (x_{b,\eta}x_{d,\eta} + y_{b,\eta}y_{d,\eta}) \frac{x_{b,\xi}^2 + y_{b,\xi}^2}{x_{b,\eta}^2 + y_{b,\eta}^2} \tag{A18}$$

and S has been defined in Part I (see Appendix).

Boundary conditions

Introducing Eqs. (11) and (12), we obtain the following linearized boundary conditions for the stability problem. Along the air-liquid interface the linearized stress balance is

$$\mathbf{n}_d \cdot (-P_b \mathbf{I} + \boldsymbol{\tau}_b) + \mathbf{n}_b \cdot (-P_d \mathbf{I} + \boldsymbol{\tau}_d) = \frac{2\kappa_d}{Ca} \mathbf{n}_b + \frac{2\kappa_b}{Ca} \mathbf{n}_d. \tag{A19}$$

This is used to replace the corresponding terms in Eq. (A8) in the surface integrals for the corresponding boundaries. Here, \mathbf{n}_b and \mathbf{n}_d denote the outward unit normal vector to the base state profile of the corresponding liquid-air interface and its disturbance, respectively. Similarly, $2\kappa_b$ and $2\kappa_d$ denote the mean curvature of the corresponding liquid-air interface at the base state and its disturbance, respectively. Along the liquid-air interfaces, we also impose the kinematic condition

$$\mathbf{n}_b \cdot \left(\mathbf{u}_d - \frac{\partial \mathbf{x}_d}{\partial t} \right) + \mathbf{n}_d \cdot \mathbf{u}_b = 0. \tag{A20}$$

This expression is used for determining the position of the mesh nodes along the liquid-air interfaces by introducing it as a boundary condition for the mesh generation equations; i.e., see Eq. (A4) in Part I. Along the solid surface, we simply impose that the velocity disturbances are equal to zero.

APPENDIX B: ALGORITHM FOR TRACKING THE CRITICAL MODE

In order to track the critical value of the Reynolds number as the Bloch wavenumber Q is varied, we employ a Newton-like algorithm similar to the one proposed by Hackler *et al.* [37]. The algorithm we use is given below.

- (1) Solve the steady state problem for a specific value of the Reynolds number:

$$R(\mathbf{v}; \text{Re}) = 0. \tag{B1}$$

- (2) Solve the eigenvalue problem for a specific value of the Bloch wavenumber, Q , for this value of Re :

$$A(\mathbf{v}; \text{Re})\mathbf{w} = \lambda M(\mathbf{v}; \text{Re})\mathbf{w}. \tag{B2}$$

(3) Find the eigenvalue with the largest growth rate of the problem:

$$\lambda_{\text{dang}} = \{\max[\text{Real}(\lambda_i)], i \in \mathbb{N} | i \leq \text{rank}(\mathbf{A})\}. \quad (\text{B3})$$

(4) Identify the corresponding eigenvector as

$$\mathbf{w}_{\text{trial}} = \mathbf{w}_{\text{dang}}. \quad (\text{B4})$$

Having determined the steady state \mathbf{v} and the eigenpair $(\lambda_{\text{dang}}, \mathbf{w}_{\text{dang}})$ for a specific value of Re , we use them as an initial guess to the following iterative procedure, with k the iteration number,

(5) Set \mathbf{y}^k as the solution vector augmented with the unknown value of Re at critical conditions:

$$\mathbf{y}^k = \begin{bmatrix} \mathbf{v}^k \\ \text{Re} \end{bmatrix}. \quad (\text{B5})$$

(6) Solve the following problem to evaluate the Newton correction of the steady solution vector, $\Delta \mathbf{y}^k$:

$$\begin{bmatrix} \mathbf{A} & \frac{\partial \mathbf{R}}{\partial \text{Re}} \\ \mathbf{w}_{\text{trial}} & 0 \end{bmatrix} \Delta \mathbf{y}^k = - \begin{bmatrix} \mathbf{R}(\mathbf{v}^k; \text{Re}) \\ 0 \end{bmatrix}. \quad (\text{B6})$$

(7) Set $\mathbf{z}^k = \mathbf{y}^k + \Delta \mathbf{y}^k$.

(8) Solve the eigenvalue problem at \mathbf{z}^k :

$$\mathbf{A}(\mathbf{z}^k) \mathbf{w} = \lambda \mathbf{M}(\mathbf{z}^k) \mathbf{w}. \quad (\text{B7})$$

(9) Calculate the tangent vector, $\frac{\partial \mathbf{z}^k}{\partial s}$, of the tracked manifold, by solving the augmented system

$$\begin{bmatrix} \mathbf{A} & \frac{\partial \mathbf{R}}{\partial \text{Re}} \\ \mathbf{w}_{\text{trial}} & 0 \end{bmatrix} \frac{\partial \mathbf{z}^k}{\partial s} = - \begin{bmatrix} 0 \\ 1 \end{bmatrix}. \quad (\text{B8})$$

This system specifies that from the entire null-space of $\mathbf{A}[\text{Null}(\mathbf{A}) \equiv \{\mathbf{x} : \mathbf{A}\mathbf{x} = 0\}]$ we choose the $\frac{\partial \mathbf{z}^k}{\partial s}$ that points to the direction of $\mathbf{w}_{\text{trial}}$, while it excludes the trivial solution ($\frac{\partial \mathbf{z}^k}{\partial s} = \mathbf{0}$) as a solution of the system (B8).

(10) Solve the eigenvalue problem at the position $\mathbf{z}^k + \epsilon \frac{\partial \mathbf{z}^k}{\partial s}$:

$$\mathbf{A} \left(\mathbf{z}^k + \epsilon \frac{\partial \mathbf{z}^k}{\partial s} \right) \mathbf{w} = \lambda \mathbf{M} \left(\mathbf{z}^k + \epsilon \frac{\partial \mathbf{z}^k}{\partial s} \right) \mathbf{w}. \quad (\text{B9})$$

(11) Calculate the derivative of the eigenvalue with respect to the arc length of the tracked manifold:

$$\frac{\partial \lambda_{\text{dang}}}{\partial s} = \frac{\lambda_{\text{dang}}(\mathbf{z}^k + \epsilon \frac{\partial \mathbf{z}^k}{\partial s}) - \lambda_{\text{dang}}(\mathbf{z}^k)}{\epsilon}. \quad (\text{B10})$$

(12) Solve the 1D linear system to calculate the pseudo arc length of the manifold:

$$\Delta s = -\lambda_{\text{dang}} / \frac{\partial \lambda_{\text{dang}}}{\partial s}. \quad (\text{B11})$$

(13) Set

$$\mathbf{y}^{k+1} = \mathbf{z}^k + \frac{\partial \mathbf{z}^k}{\partial s} \Delta s; \quad (\text{B12})$$

(14) if $\Delta s > \delta$, the prespecified tolerance, repeat steps (5)–(13).

When convergence is achieved the vector \mathbf{y}^{k+1} will contain the computed value of the critical Re number and the corresponding steady state. Given a good initial guess, this algorithm converges quadratically even if the calculated solution lies close to the hysteresis loop. After the algorithm

converges, we increase Q at $Q + dQ$ and use the calculated eigenvector of the previous step as the w_{trial} of the current step and repeat steps (5)–(14).

Although this algorithm requires four LU decompositions per iteration and thus it may not be as efficient as others that exist in the literature, e.g., [57], it is much easier to implement. The perturbation parameter that has been used in the algorithm is $\epsilon = 10^{-5}$ and the algorithm terminates when Δs is smaller than $\delta = 10^{-7}$.

-
- [1] G. M. Sisoiev, O. K. Matar, and C. J. Lawrence, Absorption of gas into a wavy falling film, *Chem. Eng. Sci.* **60**, 827 (2005).
 - [2] V. Bontozoglou, A numerical study of interfacial transport to a gas-sheared wavy liquid, *Int. J. Heat Mass Transfer* **41**, 2297 (1998).
 - [3] D. Pettas, G. Karapetsas, Y. Dimakopoulos, and J. Tsamopoulos, Viscoelastic film flows over an inclined substrate with sinusoidal topography. I. Steady state, *Phys. Rev. Fluids* **4**, 083303 (2019).
 - [4] T. B. Benjamin, Wave formation in laminar flow down an inclined plane, *J. Fluid Mech.* **2**, 554 (1957).
 - [5] C.-S. Yih, Stability of liquid flow down an inclined plane, *Phys. Fluids* **6**, 321 (1963).
 - [6] S. Kalliadasis, C. Ruyer-Quil, B. Scheid, and M. G. Velarde, *Falling Liquid Films* (Springer, London, 2012).
 - [7] G. Karapetsas and V. Bontozoglou, The primary instability of falling films in the presence of soluble surfactants, *J. Fluid Mech.* **729**, 123 (2013).
 - [8] G. Karapetsas and V. Bontozoglou, The role of surfactants on the mechanism of the long-wave instability in liquid film flows, *J. Fluid Mech.* **741**, 139 (2014).
 - [9] S. Kalliadasis and G. M. Homsy, Stability of free-surface thin-film flows over topography, *J. Fluid Mech.* **448**, 387 (2001).
 - [10] C. Bielarz and S. Kalliadasis, Time-dependent free-surface thin film flows over topography, *Phys. Fluids* **15**, 2512 (2003).
 - [11] M. Vlachogiannis and V. Bontozoglou, Experiments on laminar film flow along a periodic wall, *J. Fluid Mech.* **457**, 133 (2002).
 - [12] K. Argyriadi, M. Vlachogiannis, and V. Bontozoglou, Experimental study of inclined film flow along periodic corrugations: The effect of wall steepness, *Phys. Fluids* **18**, 012102 (2006).
 - [13] S. J. D. D'Alessio, J. P. Pascal, and H. A. Jasmine, Instability in gravity-driven flow over uneven surfaces, *Phys. Fluids* **21**, 062105 (2009).
 - [14] C. Heining and N. Aksel, Effects of inertia and surface tension on a power-law fluid flowing down a wavy incline, *Int. J. Multiphase Flow* **36**, 847 (2010).
 - [15] T. Pollak and N. Aksel, Crucial flow stabilization and multiple instability branches of gravity-driven films over topography, *Phys. Fluids* **25**, 024103 (2013).
 - [16] Y. Trifonov, Stability of a film flowing down an inclined corrugated plate: The direct Navier-Stokes computations and Floquet theory, *Phys. Fluids* **26**, 114101 (2014).
 - [17] Z. Cao, M. Vlachogiannis, and V. Bontozoglou, Experimental evidence for a short-wave global mode in film flow along periodic corrugations, *J. Fluid Mech.* **718**, 304 (2013).
 - [18] M. Schörner, D. Reck, N. Aksel, and Y. Trifonov, Switching between different types of stability isles in films over topographies, *Acta Mech.* **229**, 423 (2018).
 - [19] M. Schörner and N. Aksel, The stability cycle—A universal pathway for the stability of films over topography, *Phys. Fluids* **30**, 012105 (2018).
 - [20] S. Millet, V. Botton, F. Rousset, and H. Ben Hadid, Wave celerity on a shear-thinning fluid film flowing down an incline, *Phys. Fluids* **20**, 031701 (2008).
 - [21] C. Ruyer-Quil, S. Chakraborty, and B. S. Dandapat, Wavy regime of a power-law film flow, *J. Fluid Mech.* **692**, 220 (2012).
 - [22] M. H. Allouche, V. Botton, S. Millet, D. Henry, S. Dagois-Bohy, B. Güzel, and H. Ben Hadid, Primary instability of a shear-thinning film flow down an incline: Experimental study, *J. Fluid Mech.* **821**, (2017).

- [23] A. S. Gupta, Stability of a visco-elastic liquid film flowing down an inclined plane, *J. Fluid Mech.* **28**, 17 (1967).
- [24] F. Kang and K. P. Chen, Nonlinear elastic instability of gravity-driven flow of a thin viscoelastic film down an inclined plane, *J. Non-Newton. Fluid Mech.* **57**, 243 (1995).
- [25] W. Lai, Stability of an elastic-viscous liquid film flowing down an inclined plane, *Phys. Fluids* **10**, 844 (1967).
- [26] E. S. G. Shaqfeh, R. G. Larson, and G. H. Fredrickson, The stability of gravity driven viscoelastic film-flow at low to moderate Reynolds number, *J. Non-Newton. Fluid Mech.* **31**, 87 (1989).
- [27] R. G. Larson, Instabilities in viscoelastic flows, *Rheol. Acta* **31**, 213 (1992).
- [28] L. Dávalos-Orozco, Stability of thin viscoelastic films falling down wavy walls, *Interfacial Phenom. Heat Transfer* **1**, 301 (2013).
- [29] N. Phan-Thien, A nonlinear network viscoelastic model, *J. Rheol.* **22**, 259 (1978).
- [30] H. J. Pain, *The Physics of Vibrations and Waves*, 6th ed. (Wiley, Chichester, 2008).
- [31] K. N. Christodoulou, Computational Physics of Slide Coating Flow, Volumes I and II, Ph.D. Thesis, University of Minnesota, 1990, https://primo.lib.umn.edu/primo-explore/fulldisplay?docid=UMN_ALMA21500090920001701&context=L&vid=TWINCITIES&lang=en_US&search_scope=mncat_discovery&adaptor=Local%20Search%20Engine&tab=article_discovery&query=any,contains,computational%20physics%20of%20slide%20coating%20flow%20,%20christodoulou%20kostas%20nikiforos&offset=0.
- [32] K. N. Christodoulou and L. E. Scriven, Finding leading modes of a viscous free surface flow: An asymmetric generalized eigenproblem, *J. Sci. Comput.* **3**, 355 (1988).
- [33] G. Karapetsas and J. Tsamopoulos, On the stick-slip flow from slit and cylindrical dies of a Phan-Thien and Tanner fluid model. II. Linear stability analysis, *Phys. Fluids* **25**, 093105 (2013).
- [34] D. Pettas, G. Karapetsas, Y. Dimakopoulos, and J. Tsamopoulos, On the origin of extrusion instabilities: Linear stability analysis of the viscoelastic die swell, *J. Non-Newtonian Fluid Mech* **224**, 61 (2015).
- [35] R. Natarajan, An Arnoldi-based iterative scheme for nonsymmetric matrix pencils arising in finite element stability problems, *J. Comput. Phys.* **100**, 128 (1992).
- [36] R. B. Lehoucq, D. C. Sorensen, and C. Yang, *ARPACK Users' Guide: Solution of Large-Scale Eigenvalue Problems with Implicitly Restarted Arnoldi Methods* (SIAM, Philadelphia, 1998).
- [37] M. A. Hackler, N. C. Brandon, R. I. Hirshburg, and K. N. Christodoulou, Coatable splice process in film coating: A fluid mechanical stability problem, *AIChE J.* **43**, 3133 (1997).
- [38] N. Aksel and M. Schörner, Films over topography: From creeping flow to linear stability, theory, and experiments, a review, *Acta Mech.* **229**, 1453 (2018).
- [39] D. Tseluiko, M. G. Blyth, and D. T. Papageorgiou, Stability of film flow over inclined topography based on a long-wave nonlinear model, *J. Fluid Mech.* **729**, 638 (2013).
- [40] T. B. Benjamin, The development of three-dimensional disturbances in an unstable film of liquid flowing down an inclined plane, *J. Fluid Mech.* **10**, 401 (1961).
- [41] H. K. Ganpule and B. Khomami, An investigation of interfacial instabilities in the superposed channel flow of viscoelastic fluids, *J. Non-Newtonian Fluid Mech.* **81**, 27 (1999).
- [42] A. M. Grillet, A. C. B. Bogaerds, G. W. M. Peters, and F. P. T. Baaijens, Stability analysis of constitutive equations for polymer melts in viscometric flows, *J. Non-Newtonian Fluid Mech.* **103**, 221 (2002).
- [43] M. Schörner, D. Reck, and N. Aksel, Stability phenomena far beyond the Nusselt flow—Revealed by experimental asymptotics, *Phys. Fluids* **28**, 022102 (2016).
- [44] M. Pavlidis, G. Karapetsas, Y. Dimakopoulos, and J. Tsamopoulos, Steady viscoelastic film flow over 2D Topography: II. The effect of capillarity, inertia and substrate geometry, *J. Non-Newtonian Fluid Mech.* **234**, 201 (2016).
- [45] P.-K. Nguyen and V. Bontozoglou, Steady solutions of inertial film flow along strongly undulated substrates, *Phys. Fluids* **23**, 052103 (2011).
- [46] S. Tsouka, Y. Dimakopoulos, and J. Tsamopoulos, Stress-gradient induced migration of polymers in thin films flowing over smoothly corrugated surfaces, *J. Non-Newtonian Fluid Mech.* **228**, 79 (2016).
- [47] M. Becerra and M. S. Carvalho, Stability of viscoelastic liquid curtain, *Chem. Eng. Process.* **50**, 445 (2011).

- [48] A. V. Borkar, J. A. Tsamopoulos, S. A. Gupta, and R. K. Gupta, Spin coating of viscoelastic and nonvolatile fluids over a planar disk, *Phys. Fluids* **6**, 3539 (1994).
- [49] D. E. Bornside, C. W. Macosko, and L. E. Scriven, Spin coating of a PMMA/chlorobenzene solution, *J. Electrochem. Soc.* **138**, 317 (1991).
- [50] M. H. Allouche, S. Millet, V. Botton, D. Henry, H. Ben Hadid, and F. Rousset, Stability of a flow down an incline with respect to two-dimensional and three-dimensional disturbances for Newtonian and non-Newtonian fluids, *Phys. Rev. E* **92** (2015) 063010.
- [51] M. Dauth and N. Aksel, Breaking of waves on thin films over topographies, *Phys. Fluids* **30**, 082113 (2018).
- [52] D. Pettas, G. Karapetsas, Y. Dimakopoulos, and J. Tsamopoulos, On the degree of wetting of a slit by a liquid film flowing along an inclined plane, *J Fluid Mech.* **820**, 5 (2017).
- [53] S. Varchanis, Y. Dimakopoulos, and J. Tsamopoulos, Steady film flow over a substrate with rectangular trenches forming air inclusions, *Phys. Rev. Fluids* **2**, 124001 (2017).
- [54] N. E. Bixler, Stability of Coating Flow, Ph.D. Thesis, University of Minnesota, 1982, https://primo.lib.umn.edu/primo-explore/fulldisplay?docid=UMN_ALMA21458583540001701&context=L&vid=TWINCITIES&lang=en_US&search_scope=mncat_discovery&adaptor=Local%20Search%20Engine&tab=article_discovery&query=any,contains,bixler%20coating&offset=0.
- [55] K. J. Ruschak, A three-dimensional linear stability analysis for two-dimensional free boundary flows by the finite-element method, *Comput. Fluids* **11**, 391 (1983).
- [56] D. J. Coyle, The fluid mechanics of roll coating: Steady flows, stability and rheology, Ph.D. Thesis, University of Minnesota, 1984, https://primo.lib.umn.edu/primo-explore/fulldisplay?docid=UMN_ALMA21525090250001701&context=L&vid=TWINCITIES&lang=en_US&search_scope=mncat_discovery&adaptor=Local%20Search%20Engine&tab=article_discovery&query=any,contains,coyle%20coating.
- [57] A. G. Salinger, N. M. Bou-Rabee, R. P. Pawlowski, E. D. Wilkes, E. A. Burroughs, R. B. Lehoucq, and L. Romero, LOCA 1.0 Library of continuation algorithms: Theory and implementation manual. Sandia National Laboratories, Technical Report No. SAND2002-0396, 2002.